ISSN 0915-633X

NATIONAL INSTITUTE FOR FUSION SCIENCE

Physical Mechanism Determining the Radial Electric Field and its Radial Structure in a Toroidal Plasma

K. Ida, Y. Miura, S -I. Itoh, J.V. Hofmann, A. Fukuyama,
S. Hidekuma, H. Sanuki, H. Idei, H. Yamada, H. Iguchi, K. Itoh

(Received - May 25, 1994)

NIFS-313 Oct. 1994

RESEARCH REPORT
NIFS Series

NAGOYA, JAPAN

Physical Mechanism Determining the Radial Electric Field and its Radial Structure in a Toroidal Plasma

Katsumi Ida, Yukitoshi Miura[a], Sanae-I.Itoh[b], J.V.Hofmann[c], Atsushi Fukuyama[d], Shigeru Hidekuma, Heiji Sanuki, Hiroshi Idei, Hiroshi Yamada, Harukazu Iguchi, Kimitaka Itoh

National Institute for Fusion Science, Nagoya, 464-01, Japan

(a) Japan Atomic Energy research Institute, Ibaragi 311-01, Japan

(b) Research Institute for Applied Mechanics, Kyusyu University, 87 Kasuga, 816, Japan

(c) Max-Planck-Institute fur Plasmaphysik, Garching bei Munchen, D-85748, Germany.

(d) Faculty of engineering, Okayama University, Okayama, 700 Japan

Radial structures of plasma rotation and radial electric field are experimentally studied in tokamak, heliotron/torsatron and stellarator devices. The perpendicular and parallel viscosities are measured. The parallel viscosity, which is dominant in determining the toroidal velocity in heliotron/torsatron and stellarator devices, is found to be neoclassical. On the other hand, the perpendicular viscosity, which is dominant in dictating the toroidal rotation in tokamaks, is anomalous. Even without external momentum input, both a plasma rotation and a radial electric field exist in tokamaks and heliotrons/torsatrons. The observed profiles of the radial electric field do not agree with the theoretical prediction based on neoclassical transport. This is mainly due to the existence of anomalous perpendicular viscosity. The shear of the radial electric field improves particle and heat transport both in bulk and edge plasma regimes of tokamaks.

Keywords: radial electric field, plasma rotation, charge-exchange spectroscopy, L-mode and H-mode, TTMP damping, bifurcation of radial electric field, radial structure.

1. Introduction

1-1. Importance of an electric field

A radial electric field has been considered to possibly reduce the ripple loss and to prevent the degradation of confinement in stellarators and helical devices[1]. Efforts to study the radial electric field have been done in the Wendelstein 7A (W-7A) stellarator and the Heliotron E (H-E) devices[2,3]. In tokamaks, plasma space potential was measured for a long time, e.g., in TM-4, ISX-B[4-7]. Because no significant effects of the radial electric field on plasma confinement have been observed in the early days, few attention has been paid as a research subject in tokamaks afterwards. However, after the transition from low confinement mode (L-mode) to high confinement mode (H-mode) (L/H transition) was found in ASDEX[8], a spontaneous bifurcation of the radial electric field was theoretically proposed to cause it[9-14] and refreshed the motivation of research. The phenomenon, that associated with the L/H transition, the radial electric field suddenly changes at the plasma periphery (few cm), was observed in DIII-D[15-17], JFT-2M[18-20], ASDEX[21] and Wendelstein 7AS[22]. The H-mode could be triggered experimentally by externally inducing a radial electric field in the plasma in CCT and TEXTOR[23,24]. The importance of the radial electric field for H-mode is now widely recognized.

Thus the radial electric field has been considered to have an important effect on the confinement and anomalous transport in the plasma, and the experimental research on the mechanisms determining the radial electric field in a toroidal plasma flourished recently. Since the radial electric field is coupled with plasma rotation, research on the radial electric field is accompanying the research on the radial profile of plasma rotation. Plasma rotation results from the balance of momentum input and viscous damping. However, there exists an intrinsic rotation without external momentum input. On the other hand, the radial electric field (rotation) in the plasma affects the radial profiles of plasma density and temperature. This is because the particle transport, momentum transport and heat transport are not independent of each other but have a complex coupling[25]. Therefore, the complex plasma transport can be clarified through the research on the mechanism determining the radial electric field.

In this paper, the formation of a radial electric field is discussed, and the effect of this radial

electric field on plasma confinement is investigated. Two types of electric field formation are discussed, externally driven and internally driven. As an example of external driven electric field, (1) the negative radial electric field caused by neutral beam injection and (2) the positive radial electric field induced by electron cyclotron heating are studied. In these studies our emphasis is to clarify how the difference of magnetic field configuration (for instance tokamak and heliotron/torsatron) affects the formation of the radial electric field and plasma rotation. The plasma viscosity, which is the key parameter to determine the radial profile of the plasma rotation, is discussed in detail in this paper. For the intrinsic case, the radial electric field in L-mode and H-mode is described in detail. The effect of the radial electric field on plasma confinement is described mainly for plasmas of the counter-NBI mode and of the H-mode type; the particle and energy confinement of core and edge plasma are discussed. The mechanisms determining the radial electric field are summarized with the discussions of these experimental researches.

1-2. Basic equation to determine the structure of radial electric field and the plasma rotation

The radial electric field can be produced by a small difference of ion and electron density profiles. On the other hand, the radial electric field tends to reduce the difference. The radial electric field is also damped by the diffusion process. Some force is necessary to keep the difference of ion and electron densities to maintain a steady state radial electric field. The forces are for instance, the momentum input due to neutral beam injection, the plasma pressure gradient and the bipolar flux existing in the plasma. The radial electric field and plasma flow velocity in the plasma are governed by the momentum (force) balance equation[1];

$$m_i n_i \frac{\partial \mathbf{V}}{\partial t} + m_i n_i \mathbf{V}\cdot\nabla\,\mathbf{V} = -\nabla p - \nabla\Pi + \rho\mathbf{E} + \mathbf{j}\times\mathbf{B} + \mathbf{F}$$

Here $\mathbf{V}$ is plasma flow velocity, m_i and n_i is ion mass and density, p and Π are diagonal and off diagonal terms of pressure tensor, ρ and $\mathbf{E}$ are charge density and radial electric field, $\mathbf{j}$ and $\mathbf{B}$ are current density and magnetic field in the plasma, $\mathbf{F}$ is an external force, respectively. Here assuming the poloidal and toroidal symmetry of plasma flow, ignoring the collision term between electrons and ions, with $\rho=-en_e + eZn_i$, $\mathbf{j} = -en_e\mathbf{V_e} + eZ_in_i\mathbf{V_i}$, the force balance of ions in steady state for each direction are expressed by the following equations.

$$F_\theta = \langle \nabla_{\parallel} \Pi \rangle_\theta + \langle \nabla_{\perp} \Pi \rangle_\theta \qquad \text{poloidal direction } (\theta)$$

$$F_\phi = \langle \nabla_{\parallel} \Pi \rangle_\phi + \langle \nabla_{\perp} \Pi \rangle_\phi \qquad \text{toroidal direction}(\phi)$$

$$en_i Z_i E_r = \partial p_i / \partial r - en_i Z_i (v_\theta B_\phi - v_\phi B_\theta) \qquad \text{radial direction}(r)$$

Here, F_θ and F_ϕ are external (and internal) forces in the poloidal and toroidal directions of a toroidal plasma, respectively. The force due to the neutral beam injected in the toroidal direction (tangential direction) contributes to F_ϕ and the forces due to bipolar fluxes such as electron and ion losses work as F_θ and F_ϕ, respectively. With respect to the viscous forces, we consider two viscosities: one is the viscosity coupled to a velocity gradient in the direction parallel to the velocity and the other is the viscosity associated with a velocity gradient in the direction perpendicular to the velocity (radial direction). These viscosities are called parallel and perpendicular viscosity, and the forces are given as $<\nabla_{\parallel}\Pi>_{\theta,\phi}$ and $<\nabla_{\perp}\Pi>_{\theta,\phi}$. There are off-diagonal terms in these viscosities and the plasma rotations are not independent of temperature or density gradients (which are considered to be part of the internal forces). Taking the standard diagonal terms, the viscous forces can be expressed by the viscosity coefficients $\mu_{\parallel}^{\theta,\phi}$, $\mu_{\perp}^{\theta,\phi}$,

$$\langle \nabla_{\parallel} \Pi \rangle_{\theta,\phi} = n_i m_i \mu_{\parallel}^{\theta,\phi} V_{\theta,\phi} \qquad \text{parallel viscosity}$$

$$\langle \nabla_{\perp} \Pi \rangle_{\theta,\phi} = -n_i m_i \mu_{\perp} \nabla^2 V_{\theta,\phi} \qquad \text{perpendicular viscosity}$$

When the plasma flows in a nonuniform magnetic field, the parallel viscosity acts on it. The plasma momentum is converted to thermal energy due to the change of magnetic field strength (transit time magnetic pumping: TTMP), and the plasma velocity is damped. In tokamaks, the poloidal rotation is considered to be damped by this mechanism[26,27], since the magnetic field strength in tokamaks is proportional to the inverse of major radius. When the plasma rotates in the poloidal direction (from low field side to high field side), this rotation is damped by magnetic pumping. The magnitude of parallel viscosity is (for the 0-th order argument) large regardless of the velocity gradient. [$\mu_{\parallel}^{\theta} \approx (\pi/16)^{1/2} (r/R^2) I_p v_{th} (B/B_\theta)$[13,28], where I_p is the energy integral coefficient and

v_{th} is the thermal velocity of ions]. The measured poloidal rotation is damped and very small in L-mode operation in tokamaks[29,30]. In heliotron/torsatron, both poloidal and toroidal rotations are damped by TTMP and no large velocities are expected.

The damping force due to perpendicular viscosity is observed, when a velocity gradient exists in radial direction. Roughly speaking the toroidal rotation is peaked at the plasma center and the poloidal rotation velocity increases towards the plasma periphery. In both the poloidal and toroidal rotations, the perpendicular viscosity is important because of radial velocity gradients. In tokamaks, $\mu_{\parallel}^{\phi}=0$ due to toroidal symmetry and only $\mu_{\perp}$ is taken into account. The perpendicular viscosity coefficient is determined by solving the momentum balance equation with a force, F_{ϕ} term, due to neutral beam injection and the viscosity term. This provides an approach to simultaneously determine $\mu_{\perp}$ and spontaneous torque from the time evolution of the toroidal rotation velocity profiles. On the other hand, in studying the toroidal rotation in the heliotron/torsatron or the poloidal rotation in tokamaks, both the parallel and perpendicular viscosities $\mu_{\parallel}$, $\mu_{\perp}$ should be taken into account. The contributions of $\mu_{\parallel}$ and $\mu_{\perp}$ can be estimated by solving the diffusion equation separately for low and high magnetic field ripple.

1-3. Physical mechanisms to determine the radial structure of the electric field

Figure 1 shows schematically physical mechanisms and relations to determine the radial electric field in toroidal plasmas. The radial electric field is associated with toroidal and poloidal rotation velocities and the ion pressure gradient. There are two types of forces to drive plasma rotation in the toroidal or poloidal direction; one is the force due to the neutral beam injection and the other is bipolar flux due to electron or ion diffusion across the magnetic field. When the radial electric field is caused by NBI, the radial electric field profiles are mainly determined from the radial profiles of toroidal rotation velocity driven by the neutral beam injection through the radial momentum balance equation. However, when the radial electric field is driven by the plasma bipolar fluxes, the radial electric field is determined in a different way. This is because these bipolar fluxes have a strong electric field dependence. In the steady state, where the ion flux is equal to the electron flux, the bipolar fluxes of electrons and ions cancel each other. Therefore the magnitude of the radial electric field is not determined by the magnitude of plasma particle fluxes but by the different dependence of

these fluxes on the electric field for electrons and ions.

If there is no difference of the electric field dependence of the ion and electron fluxes, the radial electric field is determined by the boundary condition alone, yielding a trivial solution. However, if there is a difference of the electric field dependencies between ion and electron fluxes, the radial electric field is determined by the ambipolarity condition requesting equal ion and electron fluxes in steady state. When the driving force for plasma rotation does not depend on the electric field, the electric field is determined by the momentum balance equation, and when it depends on the electric field, the electric field is determined by the ambipolar condition. There are many approaches to control a radial electric field, namely by driving plasma rotation with neutral beam injection into the plasma, by controlling ion and electron losses with NBI or ECH, by changing the electric field dependence through the control of bulk temperature and density gradients. In this paper, the radial electric field profiles controlled by various approaches are presented and the physics involved in these processes are discussed.

2. Diagnostic

2-1. Electric field measurements with charge exchange spectroscopy

There are two approaches to measure an electric field: the heavy ion beam probe and the spectroscopic measurement of plasma rotation. In H-mode research, which requires a high spatial resolution, detailed plasma rotation profiles are measured using charge exchange spectroscopy (CXS) It has been demonstrated experimentally that the radial electric field measured with a heavy ion beam probe agrees with that estimated from plasma rotation[6].

The radial electric field can be estimated from plasma rotation velocity and pressure gradients using the radial force balance relation described above. In order to obtain a detailed radial profile of the electric field, high spatially resolved measurements on radial profiles of toroidal and poloidal rotation velocities and ion temperature and density are required. The most appropriate measurement technique of these parameters is charge exchange spectroscopy. In this technique, the ion temperature and plasma rotation velocity are measured from Doppler width and shift of visible radiation due to charge exchange reactions between fully stripped impurities in the plasma and fast neutral beam

atoms[31-36]. Since plasma rotation is usually measured from intrinsic impurity ions, the force balance equation for this impurity species has to be used instead of the bulk ions. CXS measurements on the bulk ions are complicated by a strong so called "cold component", radiation originating from the same ion species but from the cold plasma periphery. This cold component is much weaker in case of impurities, especially high Z impurities. Therefore, rotation velocity can be measured to a higher accuracy on high Z impurities. In the estimation of the radial electric field, the diamagnetic drift velocity v_{di} [$= 1/(en_iZ_iB_\phi)\partial p_i/\partial r$] of the bulk ions is large and comparable to the poloidal rotation velocity, but the diamagnetic drift velocity v_{dI} of the impurities is smaller by Z_I/Z_i if $\partial p_i/\partial r = \partial p_I/\partial r$ and negligible in most cases. In general, measurements with higher Z impurities yields better accuracy, because rotation velocity measurements have better accuracy than pressure gradient measurements.

2-2. Charge exchange spectroscopy

Charge exchange spectroscopy has the advantage of providing multi-chord data when using optical fibers and thus gives a high spatial resolution up to 5mm (in JFT-2M CXS). Charge exchange collisions between fully stripped impurity ions of the plasma and fast hydrogen atoms from neutral beam result in excited ions with one more electron in upper levels. For carbon impurities this process is expressed as

$$H^0(\mathrm{NB}) + C^{6+} \rightarrow H^+ + C^{5+}(n,l)$$
$$\rightarrow H^+ + C^{5+}(n',l') + h\nu \qquad : n' < n$$

For our measurements we use the C^{5+} (n=8-7) transition at λ = 529.05nm. The emission cross section for this transition at the impact energy of 40 keV is smaller than that for the n=7-6 transition (343.37nm) by a factor of three[37].However, the n=8-7 transition (529.05nm) has the advantage of lower attenuation through our optical fiber, and of a larger Doppler shift, of an absence of interfering impurity lines nearby and it is used in many tokamaks and helical devices. Principally, in this kind of measurement the emission originates from the volume defined by the intersection of the neutral beams and the line of sight. However, radiation from the plasma periphery due to the charge

exchange of impurities with thermal hydrogen atoms ("cold component") is superimposed. Due to the low temperature in the plasma periphery this emission exhibits a smaller Doppler broadening and can thus be distinguished from the more central ("hot") radiation. In order to correctly determine and eliminate this cold component, two sets of optical fiber arrays looking on and off the neutral beam line are used[38].

2-3. Multi-chord charge exchange spectroscopy

a) Spectrometer

Multi-chord measurements can be done relatively easily by combining a spectrometer with an optical fiber array and a two dimensional detector. Figure 2 shows a schematic diagram of a multi-chord measurement. An optical fiber array is arranged parallel to the entrance slit of a Czerny-Turner spectrometer and a two dimensional detector is arranged at the exit plane. This results in a spectral dispersion in the horizontal direction and a spatial resolution in the vertical direction.

b) CCD detector and video signal

The size of our CCD in the direction of wavelength is 6mm (243 channels), corresponding to a spectral range of 2.4nm which is simultaneously measured for an 1 m spectrometer with 2160 groves/mm grating. A frame transfer CCD with 60 Hz interlaced scan is used to avoid a mechanical shutter for charge transfer (60 Hz scan rate is too fast compared to the open/close time of mechanical shutter). The signal of the CCD is a standard video signal in NTSC and has 262+1/2 lines per frame. The interlaced scan starts from the left edge and ends in the middle of CCD detector in odd frame while it starts from the middle and ends at the right edge of the CCD detector in even frame as shown Fig.2. One line has 256 data sampled with 5MHz clock and 12 bit dynamics. Since one frame has 64K data, 16 frames (267ms) can be stored with 1M word memory.

c) Image intensifier (I.I.)

The spectra of each optical fiber are obtained simultaneously. A CCD camera with image intensifier (I.I) is used for the two dimensional detector. Because of the weak signal of a standard CCD an image intensifier (I.I.) is coupled to the CCD. Electrons emitted from the

photo cathode of the entrance window are intensified up to a factor of 10000 by a micro channel plate and accelerated onto a phosphor screen. The image at the phosphor screen is fiber optically transferred to the CCD.

d) CAMAC interface

A data acquisition system with a workstation + CAMAC interface is used to analyze the large amount of data. Figure 3 shows the data acquisition system of the JFT-2M multi chord charge exchange spectroscopy. The high voltage for the micro channel plate can be set with a digital analog converter (DAC) and the gain monitor is read with a data logger (DLOG). The wavelength of the spectrometer is controlled through a GPIB interface and the absolute value of the wavelength is read out by an encoder and stored into an input register (INREG). These CAMAC modules are controlled by a VAX workstation through a parallel bus crate controller (PBCC).

e) Frame window

When the Doppler width + shift of the charge exchange line is smaller than the coverage of detector, we are able to save more frames in the available digitizer memory by not digitizing and saving horizontal lines that correspond to wavelengths outside the region of interest [frame window, see Fig.4.]. This frame window circuit can provide synchronized scans to the plasma discharge. Figure 4 shows the block diagram of the frame window circuit which produces the pretrigger for the reset of the CCD camera with the main trigger of the tokamak (heliotron/torsatron) device. The CCD pretrigger is a few to a few tens of frames before the ADC start trigger. The number of frames is counted with a vertical synchronized signal (V.SYNC) of the CCD camera controller (I.I/TV controller). The frame window detects the start of each TV line with a horizontal synchronized signal (H.SYNC) and sends the sampling clock to the ADC in order to digitize the part of interest (spectral range). The clock for the setup of the ADC is created independently from a 5MHz fundamental clock. The time during which we can take data can be expanded by a factor of two to three by not digitizing the part that is not useful.

3. Plasma rotation and electric field

3-1. External drive of plasma rotation (electric field) and damping due to viscosity

3-1-1. Drive of toroidal rotation due to tangentially injected neutral beam and the damping due to viscosity

The effect of a neutral beam on the radial electric field is different in tokamaks and helical devices. In helical devices, a strong parallel viscosity is present because of a lack of toroidal symmetry. Therefore, control of an electric field through an induced toroidal rotation is complicated.In tokamaks, on the other hand, the effect of parallel viscosity on toroidal rotation is negligible and toroidal rotation is consequently determined by the perpendicular viscosity and a large toroidal rotation and electric field can be produced by tangential neutral beam injection.

A. Tokamak (negligible parallel viscosity)

JFT-2M is a tokamak with major radius R=1.3m and minor radius a=0.33m . It has two tangential neutral beams; one is parallel (co-injection) and the other is anti-parallel (counter-injection) to the plasma current. We can switch the neutral beams from co-injection to counter-injection during a discharge to induce a positive or negative radial electric field. These series of experiments were done under the conditions of a toroidal field of B_t = 1.3 T, a plasma current of I_p = 240 kA, a deuterium working gas, a limiter configuration, an elongation of κ = 1.2 and a NBI power of 0.5-0.6 MW. Figure 5(a) shows a time evolution of the toroidal rotation velocity at the plasma center in this experiments. Due to an offset of co- and counter-rotation between 560 and 610ms, the perpendicular viscosity is determined from the temporal evolution of the toroidal rotation after the switch from co- to counter- or counter- to co- injection. In tokamaks, the toroidal magnetic field ripple is small enough that the damping of toroidal rotation by TTMP (transit time magnetic pumping) can be neglected but the radial diffusion of toroidal momentum due to the perpendicular viscosity is the dominating effect[39-45].

Figure 5(b) shows the radial profile of perpendicular viscosity from a transport analysis for toroidal rotation purely damped by the perpendicular viscosity. Similar profiles of perpendicular viscosity are obtained both for discharges switched from co- to counter-injection and counter -to co-

injection. The perpendicular viscosity for counter- to co-injection is slightly smaller than that for the other one, which is due to the density peaking at the counter-injection phase. The $v_\phi = 0$ line is determined from the spectra of two sets of optical fiber arrays viewing the plasma from opposite directions (on and off the neutral beam line). These transport analyses also show the existence of an offset momentum in the counter direction. It is still open to question which mechanism produces this offset momentum in counter direction. However, preliminary transport analysis based on the assumption that the offset momentum is driven by the ion temperature gradient, was reported[46]. The offset of toroidal rotation will be described later.

The perpendicular viscosity on axis in JFT-2M is $0.1 m^2/s$ which is relatively small compared to the viscosities measured in a heliotron/torsatron described later. Therefore, toroidal rotation and radial electric field profiles can easily be controlled by the tangential neutral beam injection. Figure 6 shows radial profiles of (a) the toroidal rotation velocity and (b) the radial electric field. The central toroidal rotation velocity is 50km/s for co-injection and -100km/s for counter-injection, which is lower by a factor of two. This is due to the offset of toroidal rotation in counter direction. The offset toroidal plasma rotation is also estimated to be -25km/s from the measurement of v_ϕ with a short balanced NBI pulse in the ohmic phase. V_ϕ measurements in JFT-2M ohmic plasmas show that the plasma rotates in the counter direction with no momentum input from neutral beam injection. In L-mode discharges, the contribution of a poloidal rotation to the radial electric field is small and the radial electric field structure is mainly determined by the toroidal rotation. As can be seen from the radial force balance equation, the pressure gradient term (diamagnetic drift) contributes a negative electric field. The electric field is close to zero for co-injection because the toroidal rotation contributes a positive electric field which cancels the negative electric due to the pressure gradient term. On the other hand, a large electric field can be produced in case of counter-injection, because both the toroidal rotation term and the pressure gradient term contribute to the negative electric field. Thus, the radial electric field can be controlled by changing the direction of the neutral beam because the momentum input of this neutral beam can easily change the toroidal rotation in tokamak

B. Heliotron/torsatron device (parallel viscosity is large)

In heliotron/torsatron devices, it is difficult to produce toroidal rotation large enough to

significantly change the radial electric field because of parallel viscosity. For example, the Compact Helical System (CHS) is a heliotron/torsatron device (poloidal period number l = 2, and toroidal period number m = 8) with a major radius (R) of 95 cm and an average minor radius (a) of 20 cm[47,48]. The magnetic field ripple near the center of the helical coils (R=90-95cm) is negligible, however, it increases sharply for R >95 cm and reaches 8 % at R = 101.6 cm. Therefore the magnetic field ripple at the plasma center can be modified from zero to 8% by shifting the magnetic axis R_{ax} from 89.9cm to 101.6cm and the damping of toroidal rotation due to TTMP can be studied[49]. We note here that R_{ax} is the major radius of magnetic axis in the zero beta limit (not real position of magnetic axis) and is always smaller than the Shafranov shifted magnetic axis by a few cm in CHS[50].

Figure 7 shows the change of radial profiles of ion temperature, toroidal rotation velocity, modulation of magnetic field strength and electron density as a result of the major radius scan (R_{ax}=89.8, 94.9, 97.4cm), which is controlled by the vertical field strength in CHS heliotron/torsatron. The plasma is produced initially by electron cyclotron heating (ECH) in hydrogen gas and sustained with tangential NBI (absorbed power of 0.5 MW in the direction parallel to the helical current). The line-averaged density reaches about 2 x 10^{13} cm^{-3} after NB injection. We define the modulation of the magnetic field strength γ as $\gamma^2=<(\partial B/\partial s)^2>/B^2$, where s is the length along the magnetic field line and <> is a flux surface average operator. The structure of the magnetic field and the modulation of the magnetic field strength γ are derived from the finite-β 3-D equilibrium code VMEC[51], based on the kinetic data in the experiments. As demonstrated on the ion temperature profile, the peak position of the ion temperature, which is considered to be the plasma axis (Rp), is shifted outward due to the finite β effect and this Shafranov shift of a few cm is consistent with the prediction by VMEC. The momentum input due to the injected neutral beam has been estimated for each plasma axis (Rp) using an analytical model[52], where the parameter dependence of the shine-through, orbit loss and charge exchange loss have been involved in the model to match the result of the 3-D Monte Carlo code HELIOS[53].

As shown in Fig.7, the toroidal rotation velocities show significant damping as the magnetic axis is shifted outward (R_{ax}= 89.9 cm $\rightarrow$ 97.4cm and R_p= 91.9 cm $\rightarrow$ 98.2cm), although the energy confinement time measured with a diamagnetic loop increases from 1.5 ms (R_{ax}=89.9 cm : R_p= 91.9 cm) to 2.5 ms (R_{ax} =97.4 : R_p= 98.2cm) due to the increase of the plasma volume. Therefore the

damping of toroidal rotation at R_{ax}=97.4 cm (R_p= 98.2cm) is not due to an enhancement of radial momentum transport. In the core region $\rho < 0.5$, the plasma rotates almost parallel to the magnetic field lines, since the rotational transform in this region is 0.3 - 0.5. Several mechanisms can contribute to the damping of the parallel velocity, such as TTMP of the rotating ions due to the modulation of B (parallel viscosity), radial diffusion of momentum due to the velocity shear (perpendicular viscosity) and collisions with neutral particles (charge exchange momentum loss). Charge exchange loss becomes dominant only near the plasma edge and can be neglected in our region of interest ($\rho < 0.6$).

Figure 8 shows a the comparison between the measured plasma flow velocity parallel to the magnetic field as estimated from measured toroidal and poloidal rotation velocities and the predicted one with parallel and perpendicular viscosity. Here two discharges are analyzed for R=89.9cm and R=97.4cm, where the magnetic field ripple at the plasma center is negligible and large enough, respectively. According to neoclassical theory[26-28], the viscosity coefficient of parallel viscosity can be expressed as

$$\mu_{\parallel} = \frac{\langle B \nabla \pi \rangle}{B m_i n_i v_\phi} \sim 2\sqrt{\pi}\gamma^2 \frac{R}{M} v_{th}$$

with the modulation of the magnetic field strength γ, the major radius R, the toroidal period number M and thermal velocity v_{th}. The dashed lines in Fig.8 are predicted rotation velocities with the momentum injected into the plasma and neoclassical parallel viscosity alone. The neoclassical parallel viscosity is multiplied by 0.3 to match the measurements for R_{ax}= 97.4cm. But if the same multiplied factor for neoclassical values is used for R_{ax}= 89.9cm, the predicted parallel velocities become much larger than the measured values. This is due to the fact that the perpendicular viscosity can not be neglected for R_{ax}= 89.9cm because the parallel viscosity becomes as small as or smaller than the perpendicular one. The central rotation velocity may be explained alternatively by increasing the values of perpendicular viscosity with no parallel viscosity. To match the central parallel velocity for R_{ax}= 89.9cm a perpendicular viscosity, $\mu_\perp$ of 18m^2/s is required, which is much larger than the ion thermal diffusivity (5m^2/s)[54] and the measured parallel velocity for R_{ax}= 97.4cm can not be explained. A combination of neoclassical parallel viscosity and 3.5m^2/s perpendicular viscosity, which is comparable to ion thermal diffusivity, are required to explain the measured parallel velocity

profile both for R_{ax}= 89.9cm and R_{ax}= 97.4cm consistently. We note here that the predicted velocity profile is sensitive to $\mu_\perp$ and insensitive to $\mu_\parallel$ for R_{ax}= 89.9cm while it is sensitive to $\mu_\parallel$ and insensitive to $\mu_\perp$ for R_{ax}= 97.4cm. Thus, combination of $\mu_\parallel = \mu_\parallel^{NC}$ and $\mu_\perp = 5m^2/s$ is not arbitrary. The parallel viscosity used to explain the experimental data for R_{ax} = 97.4cm in this analysis is smaller than Shaing's formula by a factor of 0.3. The parallel viscosity depends on the three dimensional structure of magnetic field, however the viscosity discussed here is expressed only by the modulation of magnetic field ripple γ. The discrepancy of the viscosity coefficient $\mu_\parallel$ by a factor of three may come from the approximation of the high aspect ratio limit, in which the viscosity is given by the modulation of the magnetic field ripple γ alone used in Shaing's calculation, although the CHS device has low aspect ratio.

The parameter dependence of the viscosity is studied by changing the plasma density and the field ripple to check whether it is neoclassical or not. The observation confirms that the parallel viscosity is proportional to the square of the modulation of the magnetic field strength. The central parallel velocity is not determined by the parallel viscosity alone, even if the gradient of parallel velocity is zero at the plasma center. This is because the central velocity is determined by transport processes, when the perpendicular viscosity is relatively large. Here we introduce the effective parallel viscosity μ_{eff} as an indication of how strong the damping of central velocity is by parallel and perpendicular viscosities, $\mu_\parallel$ and $\mu_\perp$, in the plasma. Effective viscosity μ_{eff} is defined as $\mu_{eff}^{-1} = v_\parallel(0)m_i n_e(0)/f_{NBI}(0)$, where $f_{NBI}(0)R$ is the torque due to NBI. If there is no perpendicular viscosity this effective viscosity is equal to the parallel viscosity, $\mu_{eff} = \mu_\perp$. Figure 9 shows the inverse of the effective viscosity as a function of magnetic field ripple and electron density. The effective parallel viscosity μ_{eff} shows the γ^2 dependence as predicted by the neoclassical theory in the region where the parallel viscosity becomes dominant, $\gamma > 0.2$. When the modulation of B decreases below 0.2, the parallel velocity becomes small and perpendicular viscosity becomes dominant. As seen in Fig 8, perpendicular viscosity is dominant for $R_{ax} \leq 92.1$ cm and parallel viscosity becomes important for $R_{ax} \geq 94.9$cm. Therefore in the following discussion we assume $\mu_{eff} \approx \mu_\perp$ for $R_{ax} \leq 92.1$ and $\mu_{eff} \approx \mu_\parallel$ for $R_{ax} \geq 94.9$cm in the wide range of electron density from $0.7 \times 10^{13}/cm^3$ to $6 \times 10^{13}/cm^3$. As shown in Fig. 9(b), when the modulation of B is small ($\gamma = 0.12$), the effective viscosity shows a clear density dependence. In this case, the perpendicular viscosity is dominant and is considered to be proportional to the inverse of the electron density, because μ_{eff}^{-1} is roughly proportional to the

electron density. However, when the modulation of B becomes large ($\gamma = 0.42$), the parallel viscosity becomes dominant and there is no density dependence. Thus the perpendicular viscosity is found to decrease roughly proportional to $1/n_e$ as the global confinement is improved by increasing the electron density. This density dependence indicates the existence of anomalous radial diffusion of the momentum as observed in tokamak plasmas because the anomalous thermal diffusivity also has similar density dependence. However, the parallel viscosity does not change in this density scan experiment, confirming the plateau neoclassical prediction.

The parallel viscosity measured in CHS is smaller than the neoclassical prediction by a factor of three. In order to study this discrepancy between measurements and theoretical predictions, the toroidal rotation velocity is also studied in the Wendelstein 7-AS. The central toroidal rotation velocity is measured with single point charge-exchange spectroscopy and the measurement is line-of-sight integrated within the beam width. The present results are, however, preliminary. A detailed experimental study is in preparation. Wendelstein 7-AS has two neutral beams which provide co-, balanced- and counter-injection relative to the direction of the bootstrap current (which is opposite to the toroidal magnetic field direction). The time evolution of toroidal rotation at the plasma center measured with charge-exchange spectroscopy and the theoretical prediction are shown in Fig. 10 (a). The co-injected neutral beam starts at 0.2 sec with a power of 0.4MW, the line averaged electron density is $3\times10^{19}m^{-3}$ to $6\times10^{19}m^{-3}$, and the central ion temperature is 0.4 - 0.5 keV. As seen in Fig. 10 (a) the central toroidal rotation velocity is ≤ 5 km/s. In order to check that this toroidal rotation is due to the momentum input of the neutral beam, the toroidal rotation is also measured for a plasma with counter neutral beam injection. The measured and predicted central toroidal rotations are shown in Fig. 10 (b). Co injection (#26454) shows roughly agreement between experiment and theory, but counter injection (#26452) shows much higher velocity measured than theoretically expected. The offset of the data may be due to errors in the determination of a zero reference velocity and different deposition profiles for co- and counter-injection or a systematic error in estimating the momentum deposition profiles of co and counter neutral beams.

The parallel viscosity affects the formation of a radial electric field by neutral beam injection. Figure 11 shows the contribution of toroidal rotation and poloidal rotation to the VxB electric field, $v_\phi xB_\theta$ and $v_\theta xB_\phi$ according to the radial force balance equation for the magnetic axis at 89.9cm and 97.4cm. The contribution of toroidal rotation to the electric field is small as illustrated by the dashed

and solid lines in Fig.11 and the contribution of poloidal rotation (open and closed circles) is dominant. Therefore co neutral beam injection does not always results in positive electric field in heliotron/torsatron devices. The electric field is considered to be determined by the bipolar flux such as ion loss. The radial electric field enhanced by neutral beam injection is more negative for counter injection when the magnetic axis is shifted inward (89.9cm), although it is more negative for co injection when the magnetic axis is shifted outward (97.4cm). The tangentially injected fast ion travels toroidaly on a drift magnetic surface if the pitch angle is small enough not to be trapped in the helical ripple. The drift surface is more inside for counter traveling fast ions, while it is more outside for co traveling fast ions. More orbit loss of counter traveling fast ions is expected when the plasma surface is close to the inside vacuum vessel, and orbit loss of co traveling fast ions is expected when the plasma surface is close to outside vacuum vessel. Although there is significant difference in the density (n_e) profiles of R_{ax} = 89.9cm and R_{ax} = 97.4cm, no difference in n_e profile is observed between co and counter injection. Then the difference in the radial electric field between co and counter injection is mainly due to the direction of the fast ions and not due to the difference of NBI deposition profile. The observed radial electric field qualitatively agrees with the prediction if we assume that radial electric fields are produced by drift orbit losses of fast ions injected by neutral beams. In a tokamak, the neutral beam injection changes the toroidal rotation and a counter neutral beam always produces a more negative electric field. However, in CHS heliotron/torsatron a more negative electric field is produced at the plasma edge when larger orbit losses of fast ions are expected. The mechanism to enhance negative electric field depends on the magnetic field configuration.

3-1-2. Indirect drive of radial electric field with ECH

In stellarator plasmas with high electron temperature and low collisionality, a positive electric field determined by electron loss (electron root), is expected. In fact, a positive electric field is observed for low density ECH plasmas and a negative electric field for high density NBI plasmas[3]. In CHS, zero or negative electric field is observed for low density ($1\times10^{19}m^{-3}$) NBI plasmas and the electric field becomes more negative (ion root) as the electron density is increased. When second harmonic resonance ECH is applied to low density NBI plasmas, the electron density drops or is

clamped. As the ECH power is increased, the density drop becomes larger. The radial electric field changes its sign and suddenly becomes positive when the ECH power exceeds a critical value (90kW) as shown in Fig. 12(a)[55].There is no much difference of plasma electron density and temperature below and above the threshold (85kW and 105kW). The electron collisionality is still too large for the plasma to be in the electron root and the positive electric field is considered to be due to enhanced electron loss with ECH. This transition from ion root to electron root is observed only for the second harmonic resonance ECH focused to ripple bottom. It is not observed with 2nd resonance ECH focused to ripple top[56]. The transition from ion root to electron root in this experiment implies enhanced electron loss by ECH, because ion collisionality is not low enough for the ion root even with ECH. As shown in Figure 12 (b), the radial electric field profile with the ECH power of 85kW is almost identical to that without ECH and a positive electric field of 40V/cm is observed at the plasma periphery with the ECH power of 140kW. For a comparison with neoclassical theory, the radial electric field is calculated from the ambipolarity condition that the neoclassical ion flux has to be balanced by the neoclassical electron flux plus the ECH enhanced flux[56]. However, the radial profile of the calculated electric field shows a discrepancy with the measured one, which implies the important role of other mechanisms determining the electric field such as perpendicular viscosity, which has not been taken into account in the neoclassical theory.

3-2. Spontaneous radial electric field

A spontaneous radial electric field can exist in the plasma without external driving forces such as neutral beams or ECH. This spontaneous electric field is observed due to an offset of toroidal rotation in tokamaks, and due to a large poloidal rotation in heliotron/torsatron, or in tokamak H-modes. It is driven by the temperature and density gradients but is not consistent with the neoclassical prediction.

3-2-1. Radial profile of the radial electric field in CHS heliotron/torsatron

The spontaneous radial electric field measured in CHS heliotron/torsatron is compared with the neoclassical prediction. A 28 GHz or 53GHz gyrotron produces an ECH plasma with a low

density , while a tangential NBI with 0.9 MW can sustain the plasma at various densities (0.7 x $10^{19}m^{-3}$ to 6 x 10^{19} m^{-3}). Figure 13 shows the electron density and temperature profiles measured with Thomson scattering, ion temperature profiles measured with charge exchange spectroscopy, and the radial electric field normalized by the averaged ion temperature gradient, $T_i(0)/a$, where a is the minor radius and $T_i(0)$ is the central ion temperature. Both electron and ion temperatures are constant in the low density region (< 2 x 10^{19} m^{-3}), while the electron temperature decreases (ion temperature is unchanged) as the electron density is increased in the high density region (> 2 x 10^{19} m^{-3}), which is consistent with the fact that the energy confinement time is proportional to electron density in the low density region and tends to saturate in the high density region. The ion collisionality ν_{*i} at the half radius is 2.4 for the discharge with the electron density of 2 x 10^{19} m^{-3} and 22 for the high density discharge (n_e=6 x 10^{19} m^{-3}). The electric field at ρ = 0.8 is almost zero for the discharge with low density of 0.7 x 10^{19} m^{-3} and increases to negative values as the electron density is increased. It is -45 V/cm for n_e=2 x 10^{19} m^{-3} and -120 V/cm for n_e=6 x 10^{19} m^{-3}. Here the radial electric field E_r is normalized with respect to the averaged ion temperature gradient $T_i(0)/a$ in order to compare with the radial electric field in tokamak plasmas which have at much higher ion temperature. This normalization is equivalent to that of space potential by ion temperature, Φ/T_i in a electrostatic confined plasma. The normalized negative radial electric field in CHS increases towards the plasma periphery and its magnitude in high density discharge is larger than the edge electric field observed in L-mode discharges in JIPP TII-U tokamak [see Fig 14(b)].We observe a high magnitude radial electric field in non H-mode discharge in CHS in contrast to tokamak L-mode plasmas, which is considered to be partly due to the difference in the magnetic field structure between tokamaks and heliotron/torsatron devices, because the magnetic field structure significantly affects ion and electron losses as well as viscous damping of plasma rotation[57].

The electric field can be calculated from the ambipolarity condition using the electron and ion fluxes according to Kovrizhnykh or Hasting[58,59]. Although the predicted electric field is comparable to the measured one at the plasma core, it does not agree with the measured one near the plasma edge[60]. The neoclassical fluxes are given by temperature and density gradient alone and do not include bipolar fluxes due to charge exchange momentum loss, orbit loss of bulk or fast ions injected by neutral beams and anomalous perpendicular viscosity, which may explain this discrepancy. A comparison of measured electric field profiles with neoclassical calculations including

these mechanisms has been reported recently[61,62].

3-2-2. Radial profile of the radial electric field in L-mode plasmas

The toroidal ripple due to a finite number of toroidal field coils[63,64] localized near the plasma edge in tokamaks is much smaller than the helical ripple in heliotron/torsatron device. There should, therefore, be a difference in the spontaneous electric field in tokamaks and heliotron/torsatrons. Toroidal momentum input should be avoided to study the spontaneous electric field, although neutral beam injection is necessary to utilize charge exchange spectroscopy for plasma rotation measurements. A perpendicularly injected neutral beam is, thus, desirable for a study of the spontaneous electric field. JIPP TII-U is a tokamak with a major radius of 0.9m and a minor radius of 0.23m which has perpendicular as well as tangential neutral beams. Radial electric field profiles are measured in tangential and near perpendicular co and counterinjection experiments. Figure 14 shows radial profiles of toroidal rotation velocity and radial electric field for discharges with a neutral beam power of 0.7MW, toroidal field of 3T and central electron density of $6\times10^{19}m^{-3}$. The central toroidal rotation velocity is 40 km/s for co and -80km/s for counter parallel injection. The toroidal rotation velocity is normalized to the thermal velocity of the bulk ions to compare the magnitude of toroidal rotation for various power levels of neutral beam injection. The poloidal rotation velocity is 2-3km/s at the plasma edge (3-5 cm inside the separatrix) and the contribution of poloidal rotation to the radial electric field is relatively small. The toroidal rotation velocity contributes the radial electric field more than the poloidal rotation velocity by a factor of 2 - 3. Here, the radial electric field is normalized to the value of the central ion temperature (0.7-1.0 keV) to compare discharges with different ion temperatures. In Fig.14, "para" indicates tangential injection and "perp" perpendicular injection with an injection angle of 81 degree, and a tangential radius of 0.2m.

Since JIPP T-IIU has only one tangential and one perpendicular neutral beam, the switch from co to counter is done shot by shot in reversing the plasma current direction. As shown in Fig. 14, the plasma rotates in the direction of neutral beam injection in case of tangential injection. However it always rotates in the counter direction regardless of the direction of the neutral beam for the near perpendicular injection (-30km/s for co injection and -60km/s for counter injection). This observation shows a spontaneous rotation in the direction anti-parallel to the plasma current. This spontaneous

rotation increases as the ion temperature is increased by ICRF heating, in which no tangential momentum is injected[65,66]. The radial electric field is zero or positive for parallel neutral beam injection, while it is negative in most regions of the plasma with a peak value of -250 V/cm at half of the minor radius for the anti parallel neutral beam injection. When the neutral beam is injected perpendicularly, the spontaneous potential with respect to the plasma edge is negative and its magnitude is a few times that of Ti(0)/e for $0 < \rho < 0.5$.

3-2-3. Edge Poloidal Rotation Profiles of H-mode Plasmas

According to neoclassical theory, ion and electron radial fluxes have a different electric field dependence and the radial electric field is determined by the balance of ion and electron fluxes. When there is more than one solution for the electric field in the balance equation of the ion and electron fluxes, the radial electric field can not be determined uniquely for fixed plasma density and temperature gradients. In this situation, the radial electric field can change rapidly (without a change of other plasma parameters). This phenomenon is characterized by bifurcations between which fast transitions of the radial electric exist. In this paper, we describe two types of electric field transitions; one is the transition from small to large negative electric field as observed in tokamak H-mode and the other is the transition from ion root (negative electric field) to electron root (large positive electric field).

Since the sudden transition from low confinement (L-mode) to high confinement (H-mode) was discovered in ASDEX NBI heated plasmas, it has been observed in PDX[67], DIII-D[68], JET[69], JFT-2M[70], JIPP TII-U[71] and TFTR[72] tokamaks with ECH[73], lower hybrid resonance (LH)[74] and Ohmic[75] heating. Various theoretical models for the L to H-mode transition have been proposed since H-mode discharges were reproduced in many devices. These H-mode models are based on bipolar ion orbit losses[9-11], neoclassical viscosity[12-14], spontaneous poloidal spin-up[76] or power flow asymmetry[77] and fluctuation suppression[78]. They have been proposed to explain the sudden change of poloidal rotation velocity and radial electric field at the L/H transition.

Recently the rapid change of poloidal rotation velocity and radial electric field near the plasma periphery at the L- to H-mode transition has been reported from D-IIID[15-17] and JFT-2M[18-20]. The detail of radial electric field profiles observed in L- and H-mode plasmas in the JFT-2M tokamak

are presented in this paper. Figure 15 shows the profiles of electron temperature measured with electron cyclotron emission (ECE) and ion temperature measured with toroidaly viewing charge exchange spectroscopy before (t = 708, 742 ms) and after (t= 775, 808 ms) the L/H transition, and the edge radial electric field and edge potential profiles at ohmic (t = 692 ms), L-mode (t = 742 ms) and H-mode (t = 792 ms) phases. The discharges are with a toroidal field of 1.3 T, a plasma current of 280 kA, q_{ψ} of 2.7, a major radius of 1.3 m and a minor radius of 0.3 m and hydrogen working gas in a single null divertor configuration. The neutral beam injection (NBI) starts at 700 ms in the co-direction with a power of 0.7 MW and a second beam is added at 730 ms in the counter direction with a power of 0.3 MW to exceed the power threshold for the L/H transition which occurs at 760 ms. Both electron and ion temperature profiles show a larger pedestal at a normalized minor radius of 0.9 after the transition phase from the L-mode to the H-mode. The increase of electron temperature is simply due to the improvement of electron thermal transport, since most NBI power is deposited near the plasma center in both L-mode and H-mode phase. However the increase of central ion temperature in the H-mode phase is due to both the improvement of ion energy transport and the increase of power flow due to the collisions with electrons at higher electron density. The electric field profiles for ohmic, L-mode and H-mode plasmas are calculated from rotation velocities and pressure gradients of carbon using the momentum balance equation for impurities. The contribution of poloidal rotation to the radial electric field is dominant. The plasma always rotates in the ion diamagnetic direction outside the separatrix and in the electron diamagnetic direction inside the separatrix. The structure of poloidal flow is consistent with the measurements of phase velocity of the turbulent fluctuations in the TEXT tokamak[79]. The radial electric field is positive outside the separatrix and negative inside the separatrix. The position, where the radial electric field is zero, moves outward as the plasma changes from ohmic to L- to H-mode. The gradient of the electric field inside the separatrix is positive in the ohmic phase, almost zero in L-mode and becomes negative in the H-mode. The relative space potentials in the plasma are derived by integrating the radial electric field. Combining the measurements of space potential with electric probes, the profiles of space potential relative to the vacuum vessel for ohmic, L-mode and H-mode are obtained as shown in Fig.15(d). This negative space potential just inside the separatrix is -260 V, while the ion temperature is 170 eV at the thermal barrier.

In the following we discuss how the radial structure of the radial electric field is determined.

Since the radial electric field is connected to plasma poloidal rotation through the radial force balance equation, the transport equation for the poloidal rotation velocity determines the radial structure of electric field[20]. The neoclassical parallel viscosity is proportional to the magnitude of flow, when the poloidal rotation velocity is small enough. The parallel viscosity coefficient, Ip, which is calculated by the integration of ion energy, is around unity. However, when the poloidal rotation velocity becomes large enough so that the projection of the poloidal ExB drift velocity on the magnetic field, $v_{ExB}(B/B_\theta)$, exceeds the ion thermal velocity, the energy integration coefficient, I_p, drops below unity and the magnitude of the parallel viscosity decreases even if the poloidal velocity increases. This mechanism is the H-mode model based on neoclassical parallel viscosity[13]. We estimate the coefficient I_p for the measured poloidal rotation and check the validity of this H-mode model. The poloidal rotation velocity increases only near the plasma periphery and the velocity shear becomes large enough so that anomalous perpendicular viscosity as well as neoclassical parallel viscosity become important. The poloidal force F_θ, driving poloidal rotation (radial electric field) in JFT-2M is a j x B force due to ion orbit losses and is considered to be localized near the plasma edge, increasing exponentially towards the separatrix; $F_\theta = F_\theta(0)\exp(-c^2x^2/\rho_{pi}^2)$, where ρ_{pi} is a poloidal gyro radius. The poloidal rotation velocity profile (strictly speaking, ExB drift velocity) is determined by solving the following equation;

$$F_\theta(0)\exp\left(\frac{c^2x^2}{\rho_{\theta i}^2}\right) = \frac{\sqrt{\pi}rn_im_iv_{th}B}{4R^2B_\theta}I_pV_{ExB} - n_im_i\mu_\perp\frac{\partial^2V_{ExB}}{\partial x^2}$$

Here v_{ExB} is a ExB drift velocity defined by $ExB/|B|^2$. X is the distance from the location of the poloidal rotation peak in the mid-plane. The coefficient c is a shape factor. The poloidal force $F_\theta(0)$ is chosen to match the measured peak poloidal rotation velocity $v_{ExB}(0)$. The shape factor of the poloidal force F_θ is fixed (c = 1) in the present analysis of this paper. The boundary conditions in this calculation are $\partial v_{ExB}(0)/\partial r = 0$ and $v_{ExB}(\infty) = 0$.

Figure 16 shows the radial profile of the energy integration coefficient Ip, parallel viscosity, and perpendicular viscosity estimated from the measured poloidal rotation velocity profile. The magnitude of perpendicular viscosity required to reproduce the measured radial profile of the poloidal rotation velocity is in the range of $2m^2/s$ to $10m^2/s$. The error bar due to the uncertainty of the perpendicular viscosity coefficient is shown in Fig, 16(b). As shown in Fig 16(b), the energy

integration coefficient Ip drops below 0.5 and the parallel viscosity decreases at the plasma periphery (1cm inside the separatrix), where the poloidal rotation exceeds 10km/s. These measurements support the hypothesis of an H-mode model based on neoclassical parallel viscosity. The perpendicular viscosity increases near the plasma periphery because of the large velocity shear and its magnitude is comparable to that of parallel viscosity. In the H-mode region the perpendicular viscosity clamps the poloidal rotation together with the decreasing parallel viscosity, while the poloidal rotation is damped to small levels solely due to parallel viscosity in the L-mode region.

The poloidal force should be localized within the poloidal gyro-radius near the plasma periphery, if the Lorenz force due to orbit loss causes the poloidal force. Then the width of the velocity shear layer has been considered to be of the size of the poloidal gyro-radius. However, it can be larger than the poloidal gyro radius due to radial diffusion, when the perpendicular viscosity is as large as the parallel one as mentioned above. Figure 17 shows the width of the poloidal rotation velocity shear, $L(v_{ExB})$, defined as twice of the half width at half maximum (2xHWHM) of the poloidal rotation velocity profile estimated only inside the separatrix in the H-mode plasma. The width of the poloidal rotation velocity shear, $L(v_{EXB})$, is plotted as a function of poloidal gyro-radius. Open circles are for hydrogen plasma and closed circles are for deuterium plasma. Three lines denote the width of poloidal rotation velocity simulated from neoclassical parallel viscosity and anomalous perpendicular viscosity for three different magnitudes ($2m^2/s$, $5m^2/s$, $10m^2/s$). The width of the velocity shear layer observed in JFT-2M H-mode, is twice that of the poloidal gyro-radius and has a weak gyro radius dependence. As seen in the simulation curve, the width of poloidal rotation velocity has no poloidal gyro-radius dependence due to the anomalous perpendicular viscosity, although the poloidal force is localized within the size of a poloidal gyro-radius. When the poloidal gyro-radius becomes large (> 3cm), the perpendicular viscosity becomes less important, so that the linear dependence between the size of the poloidal rotation velocity profile and the poloidal gyro-radius becomes clear. On the other hand, when the poloidal gyro-radius becomes smaller (< 1cm), the radial transport becomes more dominant, i.e. perpendicular viscosity is as large as parallel viscosity. For the condition of the H-mode experiment in the JFT-2M tokamak discussed here, perpendicular viscosity at the peak is comparable to parallel viscosity. Therefore, the observed poloidal rotation velocity profiles in JFT-2M do not deny the validity of a H-mode model based on ion orbit losses and confirms the importance of anomalous viscosity.

When the projected poloidal velocity to the line of the magnetic field becomes large enough to exceed the ion thermal velocity (poloidal Mach number > 1), the energy integration coefficient I_p starts to decrease in the neoclassical theory. Figure 18(a) shows the poloidal Mach number versus electron density at the L-mode and H-mode phases for plasma currents of 170kA, 230kA, 280kA, with hydrogen (H) and deuterium (D) working gas. Even if the heating power is large enough, L/H transitions are not observed (the poloidal Mach number is less than unity) when the line averaged electron density is below $2x10^{19}m^{-3}$. As the line electron density is increased, the L/H transition occurs and the poloidal Mach number increases up to two and a velocity shear is produced near the plasma periphery. After the L/H transition, the electron density increases and finally the H/L transition occurs. At the H/L transition the poloidal Mach number decreases rapidly to the level in L-mode, followed by a gradual decrease of the electron density.

Fig18(b) shows the poloidal Mach number versus line averaged electron density measured in Wendelstein 7-AS L- and H-mode plasmas. Although the results are preliminary the data show a critical value of the poloidal Mach number at the L- to H-mode transition as in JFT-2M H-mode. The differences between Wendelstein 7-AS and JFT-2M H-modes are the critical line averaged density and the critical Mach number at the L to H-mode transition. The minimum line electron density to achieve H-mode in Wendelstein 7-AS is $4x10^{19}m^{-3}$ which is two times higher than that in JFT-2M. The poloidal Mach number at the L/H transition in Wendelstein 7-AS is 0.5 which is smaller than that observed in JFT-2M. As seen in the poloidal Mach numbers in JFT-2M and Wendelstein 7-AS, the H-mode in the stellarator has a qualitative similarity to the H-mode in a tokamak. Poloidal rotation and poloidal Mach number are important parameters to characterize L- and H-modes. However, the mechanism leading to a lower critical Mach number and a higher critical line averaged density in stellarators compared to tokamaks is still open to question.

4. Effects of a radial electric field on plasma confinement

4-1. Improvement of particle confinement due to a negative electric field

Since the observation of density peaking in the Alcator-C pellet injection experiments, the improvement of core confinement has been recognized to be associated with a peaked electron density

[80]. Many improved confinement modes, such as the super shot in TFTR[81], IOC-mode in ASDEX[82,83], improved L-mode in JFT-2M[84] are related to a density peaking. Recently, counter (ctr) - neutral beam (NB) heating has been found to produce peaked density profiles and to enhance the energy confinement time in ISX-B[85] and ASDEX [86,87].A density peaking model due to a radial electric field[88,89] has been proposed to explain these observations.In this paper, we compare the density peaking observed in JFT-2M with the theoretical model. According to this model, the radial flux is determined by the temperature and density gradient, radial electric field, and drift type fluctuations as;

$$\Gamma = - D\left(\frac{\partial n}{\partial r} + \frac{\alpha \partial T}{\partial r}\frac{n}{T} - \frac{eE_r}{T} n + \frac{\omega B_t}{(m/r)T} n \right)$$

where D is a diffusion coefficient, α is a numerical coefficient of order unity, ω and m/r denote the frequency and wave number of the mode for a drift-type micro-turbulence. The time evolution of density profiles calculated using the measured radial electric field and this model (solid and dashed lines) shows good agreement with the measured density profiles as shown in Fig. 19(b). The central diffusion coefficient used in this calculation is $0.02 m^2/s$. The magnitude of the diffusion coefficient is consistent with the low diffusion coefficient measured in JET[91,92]. This experiment indicates that the improved particle transport is related to the negative electric field.

4-2. Improvement of energy confinement due to a negative electric field

4-2-1. Improvement of energy confinement in the plasma core

The energy as well as particle confinement is observed to be improved by a negative electric field. The improvement of energy confinement observed in JFT-2M plasmas with a counter injected neutral beam is compared with a theoretical evaluation based on η_i-mode theory[93,94]. Figure 20(a) shows the time evolution of central ion and electron temperatures with co and counter injected neutral beams in the JFT-2M tokamak. The time evolution of the electron temperature at the center Te(0) is measured with soft X-ray pulse height analysis (PHA) with 50 ms integration time. Profiles of electron temperature and density are obtained with a 13-channel Thomson scattering (TS) system.

The co-NBI is active from 550 ms to 750 ms with an absorbed power Pabs of 0.49 MW, and the ctr-NBI is on from 750 ms to 950 ms with P_{abs} = 0.56 MW. The central toroidal rotation velocity changes its direction from co- to counter-direction 30 ms after the interchange of the neutral beam direction. The central ion temperature increases from 0.7keV to 1.1keV in the counter injection phase. The increase of the volume averaged ion temperature, $<T_i>$, as well as of the central ion temperature, indicates the improvement of global energy confinement, which is also supported by the measured energy confinement time of 18 ms for the co-NBI phase and 24 ms (1.5 times) for the ctr-NBI phase. On the other hand, the central electron temperature stays constant within 100ms after the injection of counter NBI and then starts to decrease due to increase of central radiation caused by the impurity accumulation, which is observed in the bolometer array. Finally the central ion temperature also starts to decrease due to the collisions between ions and electrons after t = 900 ms. Figure 20 (b) shows the effective thermal diffusivity estimated at the coinjection phase (t=690ms) and counter injection phase (t=890ms). The effective thermal diffusivity for the counter injection phase is reduced by the factor of three at the plasma center and 30-50% at the plasma edge relative to the co injection phase. This result is qualitatively consistent with the prediction by the η_i-mode theory. However, the radial profile of this thermal diffusivity measured is significantly different from that calculated with the η_i-mode theory, which shows that the improvement of thermal diffusivity at the counter injection phase can not be explained by the η_i-mode theory. The experiment in JFT-2M shows that the negative electric field due to counter injected neural beams causes an inward particle pinch and the peaked density profile reduces the heat and momentum transport.

We, now, discuss the effect of a radial electric field in the ECH experiments in CHS, where the radial electric field changes from negative to positive. The plasma stored energy is proportional to the electron density in the low density region as shown in Fig 21. (a). When the ECH power is increased, the electron density decreases due to enhanced particle loss and the stored energy also decreases. In Fig. 21 (b), we plot the energy confinement time normalized to electron density and root square of total absorbed power (NBI + ECH). No improvement of energy confinement is observed at the transition of the ion root (negative electric field) to electron root (positive electric field). The similar experiment with lower collisionality is carried out to study the neoclassical effect of the electric field on energy transport.

The measurements in CHS demonstrate that the plasma can be in the electron root by control

of electron loss due to second harmonic ECH. The control of the electric field by ECH will be a useful tool to study the electric field effect regardless of collisionality. To understand the technique of controlling the electric field would result in a new technique to improve plasma confinement through this radial electric field.

4-2-2. Improvement of energy confinement at the plasma periphery

The radial electric field and a poloidal rotation velocity shear are theoretically expected to reduce fluctuations in the plasma and improve the confinement[11,78,95]. We studied the relation between a poloidal rotation velocity shear and the electron and ion temperature gradients at the plasma periphery as a indication of improved confinement. Figure 22 (a) shows the radial profiles of electron and ion temperature gradients at the plasma periphery. The peak of the electron and ion temperature gradients is located 1 - 2 cm inside the separatrix, indicating that the improvement of energy confinement is just inside the separatrix. The temperature gradient for L-mode is below 40eV/cm, while it increases up to 70eV/cm for H-mode. The region of improved energy confinement is restricted to within 5 cm inside the separatrix and no improvement is observed in the plasma core region. Figure 22 (b) shows the peak electron and ion temperature gradients as a function of poloidal rotation velocity shear. Open symbols stand for L-mode and closed symbols stand for H-mode plasma. The electron and ion temperature gradients increase as the plasma current is increased. The electron and ion temperature gradients increase as the poloidal rotation velocity shear in the electron diamagnetic direction (negative electric field shear) is increased in H-mode. However, the electron and ion temperature gradients do not increase even if the poloidal velocity shear in the ion diamagnetic direction (positive electric field shear) is increased in L-mode. These observations imply the difference of the polarity dependence of electric field on energy confinement.

5. Summary

The radial electric field is connected to the plasma rotation through the radial force balance. Therefore, the radial electric field in the plasma is determined by the balance between poloidal or toroidal driving forces such as beam injection, bipolar losses due to ECH or NBI, and damping force

such as parallel and perpendicular viscosities in the plasma. The change of plasma rotation velocity profiles due to momentum input into the plasma is measured in order to study the mechanism producing a radial electric field. Parallel and perpendicular viscosity, which damp the plasma rotation, are evaluated separately. From measurements of toroidal rotation in helical devices (heliotron/torsatron and stellarator), the parallel viscosity is found to be close to the neoclassical predictions. In tokamaks, where there is almost no parallel viscosity in the toroidal direction, the experimentally determined perpendicular viscosity is found to be anomalously high.

The spontaneous electric field and plasma rotation which is generated even without external momentum input is found both in tokamak and helical plasmas. The observed radial structure of the radial electric field does not agree with the neoclassical prediction. This discrepancy is mainly due to the fact that the anomalous perpendicular viscosity in the plasma is much larger than neoclassically predicted one. The measured spontaneous plasma rotation implies the existence of off-diagonal terms in the transport matrix, since this spontaneous plasma rotation is driven by the density or temperature gradients. In H-mode plasmas, a high electric field shear, which may be caused by ion orbit losses, is observed in the plasma periphery. The detailed analysis of poloidal rotation velocity profiles in the JFT-2M tokamak H-mode shows that the perpendicular viscosity becomes as important as the parallel viscosity even for the poloidal rotation, when large velocity gradients are produced in the plasma periphery.

It has been experimentally confirmed that (1) the radial profiles of density and temperature, i.e. their gradients determined by the heat and particle transport, affect the momentum transport (radial profile of plasma rotation velocity) and that (2) the gradients of the radial electric field and/or plasma rotation affect the particle and heat transport. A particle pinch (inward flow) is experimentally found to be triggered by a negative electric field shear driven by external momentum input of a counter injected neutral beam. In H-mode plasmas, the thermal transport is reduced and large temperature gradients are produced associated with a strong negative electric field shear localized at the plasma periphery. These observations indicate the importance of off-diagonal terms between momentum transport and particle/heat transport in the transport matrix. These off-diagonal terms in the transport matrix enable us to improve the confinement by the direct (momentum injection) or indirect (heating) control of the electric field. A quantitative study of diagonal and off diagonal terms in the future will improve our understanding of anomalous transport and improved plasma

confinement.

Acknowledgement

The authors would like to thank Dr. A.Iiyoshi and Dr. M.Fujiwara for their continuous encouragements to this work. The useful discussions with Dr. A.Fujisawa and Dr.K.C.Shaing(Oak Ridge National Laboratory) are acknowledged. The authors also thank Drs. T.Hamada, K.Toi, K.Kawahata, and NBI group of JIPP T-IIU experiments, Dr. K.Matsuoka, ECH and NBI groups of CHS experiments, Dr. H.Maeda (Japan Atomic Energy Research Institute) and machine operation group of JFT-2M experiments. The authors acknowledge Dr. Matsuda (JAERI), Mr. M.Kojima and Mr. C.Takahashi for data acquisition for these experiments.

Reference

1) K.Miyamoto, Plasma physics for nuclear fusion, Iwanami, (1987).

2) H.Wobig, H.Maassberg, H.Renner, W VII-Team, ECRH Group, NI Group, in Plasma Physics and Controlled Nuclear Fusion Research (Proc. of 11th Int. Conf., Kyoto, 1986) Vol.II p.369, IAEA, Vienna (1987).

3) K.Kondo, H.Zushi, H.Nakamura, et al., Rev. Sci. Instrum, **59**, (1988) 1533.

4) K.A.Razumova, Plasma Physics and Controlled Fusion **26**, (1984) 37.

5) M.Murakami, et al., *in Plasma Physics and Controlled Nuclear Fusion Research (Proc. of 10th Int. Conf., 1984, London)*, Vol.I, p.87, IAEA, Vienna (1985).

6) G.A.Hallock, J.Mathew, W.C.Jennings and R.L.Hickok, Phys. Rev. Lett. **56** (1986) 1248.

7) G.A.Hallock, A.J.Wootoon and R.L.Hickok, Phys. Rev. Lett. **59** (1987) 1301.

8) F.Wagner, G.Becker, K.Behringer, D.Campbell, A.Eberhangen, W.Engelhardt, G.Fussmann, O,Gehre, J.Gernhardt, G.v.Gierke, G.Haas, M.Huang, F.Karger, M.Keilhacker, O.Kluber, M.Kornherr, K.Lackner, G.Lisitano, G.G.Lister, H.M.Mayer, D.Meisel, E.R.Muller, H.Murmann, H.Niedermeyer, W.Poschenrieder, H.Rapp, H.Rohr, F.Schneider, G.Siller, E.Speth, A.Stabler, K.H.Steuer, G.Venus, and O.Vollmer, Phys. Rev. Lett. **49**, (1982) 1408.

9) S.-I.Itoh and K.Itoh, Phys. Rev. Lett. **60**, (1988) 2276.

10) S.-I.Itoh and K.Itoh, Nucl. Fusion **29**, (1989) 1031.

11) S.-I.Itoh and K.Itoh, J. Phy. Soc. Jpn. **59**, (1990) 3815.

12) K.C.Shaing, et al., *in Plasma Physics and Controlled nuclear Fusion Research (Proc. 12th Int. Conf., Nice, 1988)* Vol.II, p13, IAEA Vienna, (1989).

13) K.C.Shaing and E.C.Crume Jr, Phys. Rev. Lett. **63**, (1989) 2369.

14) K.C.Shaing, E.C.Crume Jr, and W.A.Houlberg, Phys. Fluids **B2**, (1990) 1492.

15) R.J.Groebner, K.H.Burrell, and R.P.Seraydarian, Phys. Rev. Lett. **64**, (1990) 3015.

16) K.H.Burrell, T.N.Carlstrom, E.J.Doyle, P.Gohil, R.J.Groebner, T.Lehecka, N.C.Luhmann, Jr., H.Matsumoto, T.H.Osbone, W.A.Peebles, and R.Philipona, Phys. Fluids **B2**, (1990) 1405.

17) E.J.Doyle, R.J.Groebner, K.H.Burrell, P.Gohil, T.Lehecka, N.C.Luhmann, Jr., H.Matsumoto, T.H.Osborne, W.A.Peebles, and R.Philipona, Phys. Fluids **B3**, (1991) 2300.

18) K.Ida, S.Hidekuma, Y.Miura, T.Fujita, M.Mori, K.Hoshino, N.Suzuki, T.Yamauchi and JFT-2M Group, Phys. Rev. Lett. **65**, (1990) 1364.

19) K.Ida, S.Hidekuma, M.Kojima, Y.Miura, S.Tsuji, K.Hoshino, M.Mori, N.Suzuki, Phys. Fluids. **B4**, (1992) 2552.

20) K.Ida, K.Itoh, S.I.-I.Itoh, Y.Miura, JFT-2M Group, A.Fukuyama, Phys.plasma 1, (1994) 116.

21) A.R.Field et al., Nucl. Fusion **43**, (1992) 1191.

22) V.Erckmann, F.Wagner, J.Baldzuhn, R.Brakel, R.Burhenn, U.Gasparino, P.Grigull, H.J.Hartfuss, J.V.Hofmann, R.Jaenicke, H.Nidermeyer, W.Ohlendorf, A.Rudjj, A.Weller, S.D.Bogdanov, B.Bomba, A.A.Borschegovsky, G.Cattanei, A.Dodhy, D.Dorst, A.Elsner, M.Endler, T.Geist, L.Giannone, H.Hacker, O.Heinrich, G.Herre, D.Hildebrandt, V.I.Hiznyak, W.Kasparek, F.Karger, M.Kick, S.Kubo, A.N.Kufin, V.I.Kurbatov, A.Lazaros, S.A.Malygin, V.I.Malygin, K.McCormick, G.A.Muller, V.B.Orlov, P.Pech, H.Ringler, I.N.Roi, F.Sardei, S.Sattler, F.Schneider, U.Schneider, P.G.Schuller, G.Siller, U.Stroth, M.Tutter, E.Unger, H.Wolff, E.Wursching, S.Zopfel, Phys. Rev. Lett. **70**, (1993) 2086.

23) R.J.Taylor, M.L.Brown, B.D.Fried, H.Grote, J.R.Liberati, G.J.Morales, P.Pribyl, D.Darrow, and M.Ono, Phys. Rev. Lett. **63**, (1989) 2365 .

24) R.R.Weynants, and R.J.Taylor, Nucl. Fusion **30**, (1990) 945.

25) S.-I.Itoh and K.Itoh, Kakuyugou Kenkyu **67**, (1992) 136.

26) H.Stix, Phys. Fluids **16**, (1973) 1260.

27) K.C.Shaing, Phys. Fluids **B2**, (1990) 2847.

28) K.C.Shaing and J.D.Callen, Phys. Fluids **26**, 1526 (1983).

29) K.Brau, M.Bitter, R.J.Goldston, D.Manos, K.McGuire, S.Suckewer, Nucl. Fusion **23**, (1983) 1643.

30) R.D.Benjamin, J.L.Terry and H.W.Moos, Rev. Sci. Instrum. **57**, (1986) 2020.

31) R.J.Fonck, M.Finkenthal, R.J.Goldston, D.L.Herndon, R.A.Hulse, R.Kaita, D.D.Meyerhofer, Phys. Rev. Lett. **49**, (1982) 737.

32) R.J.Fonck, D.S.Darrow, and K.P.Jaehnig, Phys. Rev. **A 29**, (1984) 3288.

33) R.C.Isler, L.E.Murrary, Appl. Phys. Lett. **42**, (1983) 355.

34) R.J.Groebner, N.H.Brooks, K.H.Burrell, L.Pottler, Appl. Phys. Lett. **43**, (1983) 920.

35) K.P.Jaehnig, R.J.Fonck, K.Ida, E.T.Powwell, Rev. Sci. Instrum. **56**, (1985) 865.

36) R.P.Seraydarian, K.H.Burrell, Rev. Sci. Instrum. **57**, (1986) 2012.

37) K.Ida, T.Kato, Phys. Letter. **A166**, (1992) 35.

38) K.Ida, S.Hidekuma, Rev. Sci. Instrum. **60**, (1989) 867.

39) K.H.Burrell, R.J.Groebner, H.St.John, R.P.Seraydarian, Nucl. Fusion **28**, (1988) 3.

40) H.Weisen, M.von Hellermann, A.Boileau, L.D.Horton, W.Mandl, H.P.Summers, Nucl. Fusion **29**, (1989) 2187.

41) A.Kallenbach, H-M.Mayer, G.Fussmann, R.Buchse, O.Gruber, O.Kluber, V.Mertens, O.Vollmer, H.Zohm,Nucl. Fusion **30**, (1990) 645.

42) K.Ida, S.-I.Itoh, K.Itoh, S.Hidekuma, Y.Miura, N.Suzuki, M.Mori, T.Matsuda, T.Yamauchi, and JFT-2M Group, *in Controlled Fusion and Plasma Heating, (17th European Conf., 1990 Amsterdam),* Vol.**14B**, Part.I, p.267, European physical Society, Petit-Lancy, Switzerland, (1990).

43) R.J.Fonck, R.Howell, K.Jaehnig, et al., Phys. Rev. Lett. **63**, (1989) 520.

44) S.Scott, et al., Phys. Rev. Lett. **64**, (1990) 531.

45) J.A.Snipes, et al., Nucl. Fusion **30**, (1990) 205.

46) K.Ida, K.Itoh, S.-I.Itoh, Y.Miura, JFT-2M Group, Nation Institute for Fusion Science Report, NIFS-241.

47) K.Matsuoka et. al., *in Plasma Physics and Controlled Nuclear Fusion Research (Proc. 12th*

Conf., Nice, 1988) Vol.II, p.411, IAEA, Vienna (1989).

48) O.Kaneko, et al., *in Plasma Physics and Controlled Nuclear Fusion Research 1990 (Proc. 13th Int. Conf., Washington D.C., 1990),* Vol.II, p.473, IAEA, Vienna (1991).

49) K.Ida, H.Yamada, H.Iguchi, K.Itoh, CHS Group, Phys. Rev. Lett. **67**, (1991) 58.

50) H.Yamada, K.Ida, H.Iguchi, S.Morita, O.Kaneko, H.Arimoto, M.Hosokawa, H.Idei, S.Kubo, K.Matsuoka, K.Nishimura, S.Okamura, Y.Takeiri, Y.Takita, C.Takahashi, K.Hanatani, H.C.Howe, S.P.Hirshman, D.K.Lee, Nucl. Fusion **32**, (1992) 25.

51) S.P.Hirshman, W.van Rij, and P.Merkel, Comput. Phys. Commun. **43**, (1986) 143.

52) J.A.Rome, J.D.Callen, J.F.Clarke, Nucl. Fusion **14**, (1974) 141.

53) R.H.Fowler, R.N.Morris, J.A.Rome and K.Hanatani, Nucl. Fusion **30**, (1990) 997.

54) H.Yamada, K.Ida, H.Iguchi, H.C.Howe, S.Kubo, Y.Ogawa, K.Hanatani, D.Okamura, H.Arimoto, M.Hosokawa, H.Idei, O.Kaneko, K.Matsuoka, S.Morita, K.Nishimura, N.Noda, T.Ozaki, A.Sagara, H.Sanuki, Y.Takeiri, Y.Takita, C.Takahashi, K.Tsuzuki, *in Controlled Fusion and Plasma Heating, (Proc. 18th European Conf., Berlin),* Vol. **15C**, Part II, p.137, European Physical Society, Petit-Lancy, Switzerland, (1991).

55) H.Idei, K.Ida, H.Sanuki, et al., Phys. Rev. Lett. **71**, (1993) 2220.

56) H.Idei, K.Ida, H.Sanuki, et al., submitted to Phys. Plasma.

57) K.Ida, S.Hidekuma, K.Itoh, S.-I.Itoh, JIPP T-IIU and CHS Group, *in Plasma Physics and Controlled Nuclear Fusion Research (Proc. 13th Int. Conf., Washington D.C., 1990)* Vol.II, p.577, IAEA, Vienna (1991).

58) L.M.Kovrizhnykh, Nucl. Fusion **24**, (1984) 435.

59) D.E.Hastings, W.A.Houlberg, K.C.Shaing, Nucl. Fusion **25**, (1985) 445.

60) K.Ida, H.Yamada, H.Iguchi, S.Hidekuma, H.Sanuki, K.Yamazaki, and CHS Group, Phys. Fluids **B3**, (1991) 515 and Fluids **B4**, (1992) 1360.

61) H.Sanuki, K.Itoh, K.Ida, S.-I.Itoh, J.Phys. Soc. Jpn. **60**, (1991) 3698.

62) H.Sanuki, K.Itoh, S.-I.Itoh, J.Phys. Soc. Jpn. **62**, (1993) 123.

63) K.T.Tsang and E.A.Frieman Phys. Fluids **19**, (1976) 752.

64) K.C.Shaing and J.D.Callen Phys. Fluids **25**, (1982) 1012.

65) S.Morita, et al., in Controlled Fusion and Plasma Heating, (Proc. 14th Europ. Conf. Madrid, 1987) Vol. 11D , part III, p874, European Physical Society (1987).

66) K.Ida, K.Kawahata, K.Toi, T.Watari, O.Kaneko, Y.Ogawa, H.Sanuki, K.Adati, R.Akiyama, A.Ando, R.Ando, Y.Hamada, S.Hidekuma, S.Hirokura, A.Karita, T.Kawamoto, Y.Kawasumi, M.Kojima, R.Kumazawa, T.Kuroda, K.Masai, S.Morita, K.Narihara, K.Ohkubo, Y.Oka, S.Okajima, T.Ozaki, M.Sakamoto, M.Sasao, K.Sato, K.N.Sato, T.Seki, F.Shimpo, Y.Taniguchi, T.Tsuzuki, H.Yamada, Nucl. Fusion **31**, (1991) 943.

67) S.M.Kaye M.G.Bell, K.Bol, D.Boyd, K.Brau, D.Buchenauer, R.Budny, A.Cavallo, P.Couture, T.Crowley, D.S.Darrow, H.Eubank, R.J.Fonck, R.Goldston, B.Grek, K.P.Jaehnig, D.Johnson, R.Kaita, H.Kugel, B.LeBlanc, J.Manicam, D.Manos, D.Mansfield, E.Mazzucato, R.McCann, D.McCune, K.McGuire, D.Mueller, A.Murdock, M.Okabayashi, K.Okano, D.K.Owens, D.E.Post, M.Reusch, G.L.Schmidt, S.Sesnic, R.Slusher, S.Suckewer, C.Surko, H.Takahashi, F.Tenney, H.Towner, and J.Valley, J. Nucl. Mater **121**, (1984) 115.

68) M.Nagami, M.Kasai, A.Kitsunezaki, T.Kobayashi, S.Konoshima, T.Matsuda, M.Miya, H.Ninomiya, S.Sengoku, M.Shimada, H.Yokomizo, T.Anmgel, C.Armentrout, F.Blau, G.Bramson, N.Brooks, R.Chase, A.Colleraine, E.Fairbanks, J.Fasolo, R.Fisher, R.Groebner, T.Hino, R.Hong, G.Jahns, J.Kamperschroer, J.Kim, A.Lieber, J.Lohr, D.McColl, L.Rottler, R.Seraydarian, R.Silagi, J.Smith, R.Snider, T.Taylor, J.Tooker, D.Vaslow, and S.Wojtowicz, Nucl. Fusion **24**, (1984) 183.

69) A.Tanga, K.H.Behringer, A.E.Costley, M.Brusati, B.Denne, A.Edwards, A.Gibson, R.D.Gill, N.Gottardi, R.Granetz, P.J.Harbour, H.Jackel, M.Keilhacker, E.Lazzaro, M.Malacarne, P.D.Morgan, P.Noll, J.Orourke, P.E.Stott, D.R.Summers, J.A.Tagle, and P.R.Thomas, Nucl. Fusion **27**, (1987) 1877.

70) S.Sengoku, A.Funahashi, M.Hasegawa, K.Hoshino, S.Kasai, T.Kawakami, H.Kawashima, T.Matoba, T.Matsuda, H.Matsumoto, Y.Miura, M.Mori, H.Ogawa, T.Ogawa, H.Ohtsuka, T.Shoji, N.Suzuki, H.Tamai, Y.Uesugi, T.Yamamoto, and T.Yamauchi, Phys. Rev. Lett. **59**, (1987) 450.

71) K.Toi, K.Kawahata, S.Morita, T.Watari, R.Kumazawa, K.Ida, A.Ando, Y.Oka, M.Sakamoto, Y.Hamada, K.Adati, R.Ando, T.Aoki, S.Hidekuma, S.Hirokura, O.Kaneko, A.Karita, T.Kawamoto, Y.Kawasumi, T.Kuroda, K.Masai, K.Narihara, Y.Ogawa, K.Ohkubo, S.Okajima, T.Ozaki, M.Sasao, K.N.Sato, T.Seki, F.Shimpo, H.Takahashi, S.Tanahashi, Y.Taniguchi, and T.Tsuzuki, Phys. Rev. Lett. **64**, (1990) 1895.

72) C.E.Bush, R.J.Goldston, S.D.Scott, E.D.Fredrickson, K.McGuire, J.Schivell, G.Taylor, Cris W. Barnes, M.G.Bell, R.L.Boivin, N.Bretz, R.V.Budny, A.Cavallo, P.C.Efthimion, B.Grek, R.Hawryluk, K.Hill, R.A.Hulse, A.Janos, D.W.Johnson, S.Kilpatrick, D.M.Manos, D.K.Mansfield, D.M.Meade, H.Park, A.T.Ramsey, B.Stratton, E.J.Synakowski, H.H.Towner, R.M.Wieland, M.C.Zarnstorff, and S.Zweben, Phys. Rev. Lett. **65**, (1990) 424.

73) K.Hoshino, T.Yamamoto, H.Kawashima, N.Suzuki, Y.Uesugi, M.Mori, H.Aikawa, S.Kasai, T.Kawakami, T.Matsuda, Y.Miura, K.Odajima, H.Ogawa, T.Ogawa, H.Ohtsuka, T.Shoji, H.Tamai, T.Yamauchi, T.Kondo, I.Nakazawa, C.R.Neufeld, and H.Maeda, Phys. Rev. Lett. **63**, (1989) 770.

74) S.Tsuji, K.Ushigusa, Y.Ikeda, T.Imai, T.Itami, M.Nemoto, K.Nagashima, Y.Koida, Y.Kawano, T.Fukuda, T.Kondoh, M.Shimada, H.Nakamura, O.Naito, H.Yoshida, T.Nishitani, H.Kubo, K.Tobita, Y.Kusama, S.Ishida, M.Sato, N.Isei, T.Sugie, N.Miya, R.Yoshino, and K.Uehara, Phys. Rev. Lett. **64**, (1990) 1023 .

75) T.H.Osborne, N.H.Brooks, K.H.Burrell, T.N.Carlstrom, R.J.Groebner, W.Howl, A.G.Kellman, L.L.Lao, T.S.Taylor, D.N.Hill, N.Ohyabu, and M.E.Perry, Nucl. Fusion **30**, (1990) 2023.

76) A.B.Hassam, T.M.Antonsen Jr, J.F.Drake, and C.S.Liu, Phys. Rev. Lett. **66**, (1991) 309.

77) M.Tendler and V.Rozhansky, Comments Plasma Phys. Controlled Fusion **13**, (1990) 191.

78) H.Biglari, P.H.Diamond, and P.W.Terry, Phys. Fluids **B2**, (1990) 1.

79) Ch.P.Ritz, R.D.Bengtson, S.J.Levinson, E.J.Powers, Phys. Fluids **27**, (1984) 2965.

80) M.Greenwald, D.Gwinn, S.Milora, J.Paker, R.Parker, S.Wolfe, et al., Phys. Rev. Lett. **53**, (1984) 352.

81) J.D.Strachan et al., Phys. Rev. Lett. **58**, (1987) 1004.

82) F.X.Soldner, E.R.Muller, F.Wagner, et al., Phys. Rev. Lett. **61**, (1988) 1105.

83) K.McCormick et al., J.Nucl. Mat. **176 & 177**, (1990) 89.

84) M.Mori, N.Suzuki, et al., Nucl. Fusion **28**, (1988) 1891.

85) R.C.Isler et al., Phys. Rev. Lett. **47**, (1981) 649.

86) O.Gehre, O.Gruber, H.D.Murmann, D.E.Roberts, F.Wagner, et al., Phys. Rev. Lett. **60**, (1988) 1502.

87) V.Mertens, et al., Plasma Phys. Contl. Fusion **32**, (1990) 965.

88) S.-I.Itoh, J. Phys. Soc. Jpn. **59**, (1990) 3431.

89) R.D.Hazeltine, S.M.Mahajan, D. A. Hichcock, Phys. Fluids **24**, (1981) 1164.

90) K.Ida, S.-I. Itoh, K.Itoh, S.Hidekuma, Y.Miura, H.Kawashima, M.Mori, T.Matusda, N.Suzuki, H.Tamai, T.Yamauchi, and JFT-2M Group, Phys. Rev. Lett. **68**, (1992) 182.

91) D.Pasini, M.Mattioli, A.W.Edwards, R.Giannella, et al., Nucl. Fusion **30**, (1990) 2049.

92) R.Giannella et al., *in Controlled Fusion and Plasma Heating, (Proc. 18th European Conf., Berlin),* Vol.**15C**, Part.I, P.197, European physical Society, Petit-Lancy, Switzerland, (1991).

93) B.Coppi and C. Spight, Phys. Rev. Lett. **41**, (1978) 551.

94) F.Romanelli, Phys. Fluids **B1**, (1989) 1018.

95) K.C.Shaing, Phys. Fluids **31**, (1988) 2249.

Figure captions

Fig.1. Physical mechanisms determining the radial electric field in a toroidal plasma.

Fig.2. Schematic diagram of the multi-channel measurement using optical fiber array. Solid lines show interlace scans in the odd frame and dashed line show scans in the even frame.

Fig 3. Block diagram of data acquisition system for the multi-channel charge exchange spectroscopy.

Fig.4. Block diagram of the frame window.

Fig.5. (a) Time evolution of the toroidal rotation velocity at the plasma center and (b) radial profiles of perpendicular viscosity for a neutral beam injection experiment in the JFT-2M tokamak.

Fig.6. Radial profiles of (a) plasma toroidal rotation velocity and (b) radial electric field in co- (t=690ms) and counter-NBI phase (t=890ms) in the JFT-2M tokamak, where ρ is the normalized averaged minor radius (from Phys. Rev. Lett. 68 (1992) 182). The solid line is a fit through the data points.

Fig.7. Radial profiles of (a) ion temperature, (b) toroidal rotation velocity, (c) modulation of magnetic field strength γ (where $\gamma^2=<|\partial B/\partial s|^2>/B^2$), and (d) electron density for the major radii of 89.9cm, 94.9cm and 97.4cm in CHS heliotron/torsatron, where ρ is the normalized averaged minor radius and $\varepsilon(0)$ is the magnetic field ripple at the plasma magnetic axis (from Phys. Rev. Lett. 67 (1991) 58).

Fig.8. Comparison of radial profiles of the parallel velocity and theoretical estimates using only neoclassical parallel viscosity (dashed line), a perpendicular viscosity of $18m^2/s$ (dot-dashed lines) and a combination of parallel and perpendicular viscosity (solid line) for major radii of (a) 89.9cm and (b) 97.4cm in CHS heliotron/torsatron, where $\mu_{\parallel}^{NC}$ is neoclassical parallel

viscosity in the plateau regime. (from Phys. Rev. Lett. 67 (1991) 58).

Fig.9. Inverse effective central viscosity derived from the measured central toroidal rotation velocity, electron density and momentum input as a function of (a) the modulation of magnetic field strength at the plasma axis and (b) line averaged density in CHS heliotron/torsatron. In Fig(9a), the dashed line is an estimate by a neoclassical parallel viscosity and solid line shows the estimate by a combination of neoclassical parallel and anomalous perpendicular viscosity.

Fig.10. (a)Temporal evolution of the central toroidal rotation velocity and the prediction by neoclassical parallel viscosity for co-neutral beam injection and (b) comparison of measured central toroidal rotation velocities with the predictions by the neoclassical parallel viscosity for co, counter(ctr), and balanced(blnc) neutral beam injection in the Wendelstein 7 AS stellarator.

Fig.11. Radial profiles of the VxB electric field in plasmas with co- and counter-neutral beam injection for major radii of (a) 89.9cm and (b) 97.4cm in CHS heliotron/torsatron, where ϕ and θ stand for the toroidal and poloidal direction, respectively.

Fig.12. (a) Radial electric field at the normalized averaged minor radii ρ = 0.49, 0.61, 0.72 and 0.82 as a function of launched power of 2nd harmonic electron cyclotron resonance heating (ECH) and (b) radial profile of the electric field for the discharges without and with ECH (85kW and 140kW) in CHS heliotron/torsatron.

Fig.13. Radial profiles of (a) electron density, (b) electron temperature, (c) ion temperature (d) radial electric field for density a scan (n_e = 0.7, 2.0, 6.0, x$10^{19}m^{-3}$) in CHS heliotron/torsatron, where ρ is the normalized averaged minor radius.

Fig.14. Radial profiles of (a) toroidal rotation velocity normalized to thermal velocity and (b) normalized radial electric field for co and counter, parallel and near perpendicular neutral

beam injection in JIPP TIIU tokamak, where a is the minor radius and ρ is the normalized averaged minor radius

Fig.15. Radial profiles of (a) electron temperature measured ECE and (b) ion temperature measured with charge exchange spectroscopy, (c) radial electric field and (d) plasma space potential for ohmic (t=692ms, OH), L-mode(t=742ms) and H-mode (t=792ms) phases, where ρ is the normalized averaged minor radius and ds is the distance from the separatrix (negative: inside, positive : outside). SOL means scrape off layer. The absolute value of the space potential is measured by probes (squares symbols).(from Phys Fluids B4 (1992) 2552).

Fig.16. Radial profiles of (a) ExB drift velocity , (b) parallel and perpendicular viscosities and energy integral coefficient I_p at the plasma edge in H-mode. SOL means scrape off layer.

Fig.17. The thickness of ExB drift velocity shear as a function of poloidal gyro-radius. Open circles stand for hydrogen plasma and closed circles for deuterium plasma. Three lines show the simulated results with neoclassical parallel viscosity plus perpendicular viscosities of $2m^2/s$, $5m^2/s$ and $10m^2/s$.

Fig.18.Poloidal Mach numbers as a function of line averaged electron density in (a) the JFT-2M tokamak with plasma currents of 170kA, 230kA, 280kA for hydrogen (H) and deuterium (D) plasmas and (b) Wendelstein 7 AS stellarator.

Fig.19. (a)Time evolutions and (b) radial profiles of measured electron density (open and closed circles) for co and counter neutral beam injection in the JFT-2M tokamak compared with theoretical predictions (lines). (from Phys. Rev. Lett. 68 (1992) 182).

Fig.20. (a) Time evolution of the central electron and ion temperatures and the volume averaged ion temperature (b) radial profile of the effective thermal diffusivity compared with the prediction by η_i mode theory for co and counter neutral beam injection phases in JFT-2M tokamak. (from Phys. Rev. Lett. 68 (1992) 182).

Fig. 21. (a) Plasma stored energy as a function of line averaged density and (b) energy confinement time as a function of injected power for 2nd second harmonic resonance electron cyclotron heating in CHS heliotron/torsatron.

Fig. 22. (a) Radial profiles of the electron and ion temperature gradients at the plasma edge and (b) peak values of the electron and ion temperature gradients as a function of poloidal rotation velocity shear in the JFT-2M L- and H-mode plasmas.

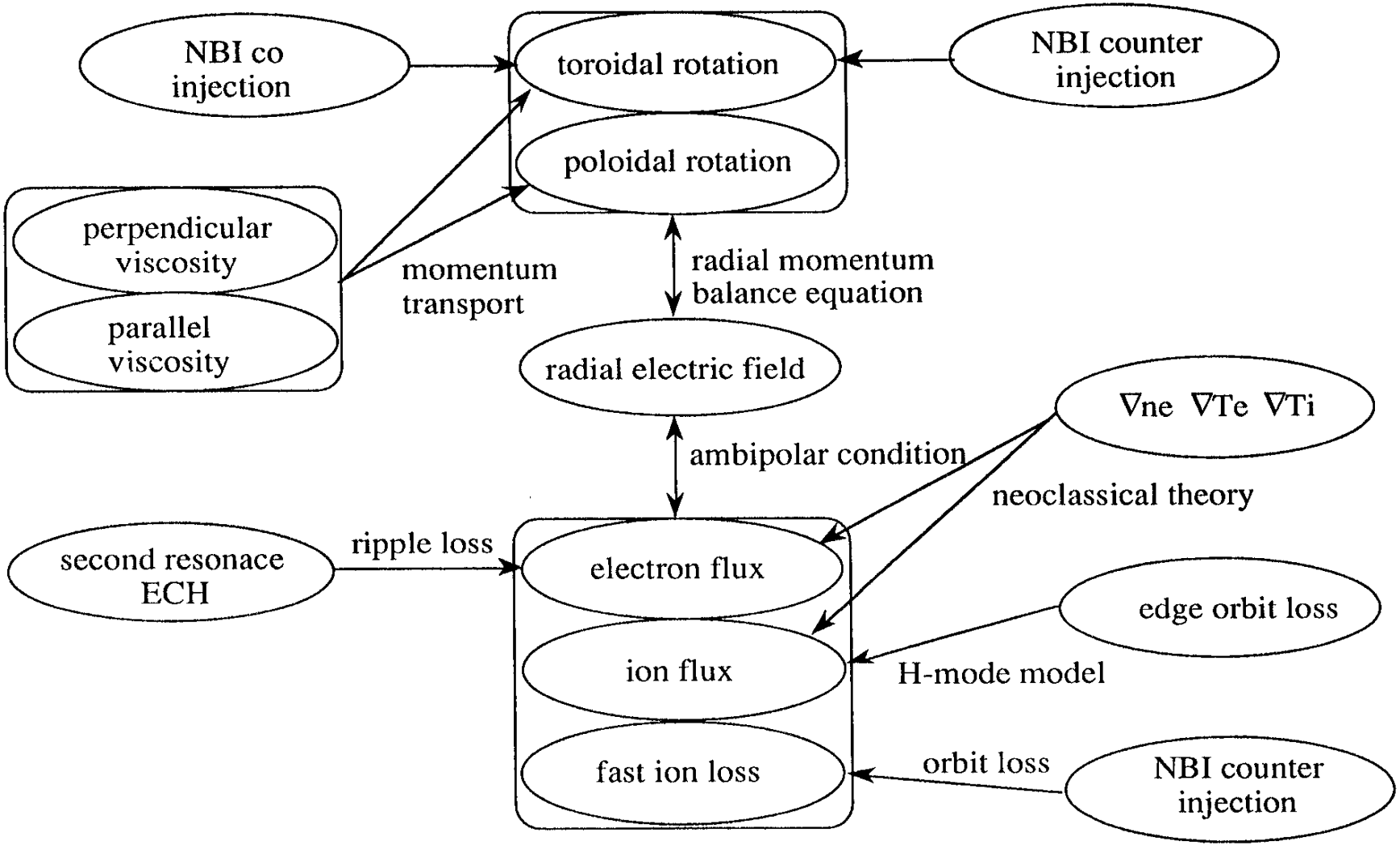
NBI co injection
toroidal rotation
NBI counter injection
poloidal rotation
perpendicular viscosity
parallel viscosity
momentum transport
radial momentum balance equation
radial electric field
∇ne ∇Te ∇Ti
ambipolar condition
neoclassical theory
second resonace ECH
ripple loss
electron flux
edge orbit loss
ion flux
H-mode model
fast ion loss
orbit loss
NBI counter injection

Fig. 1

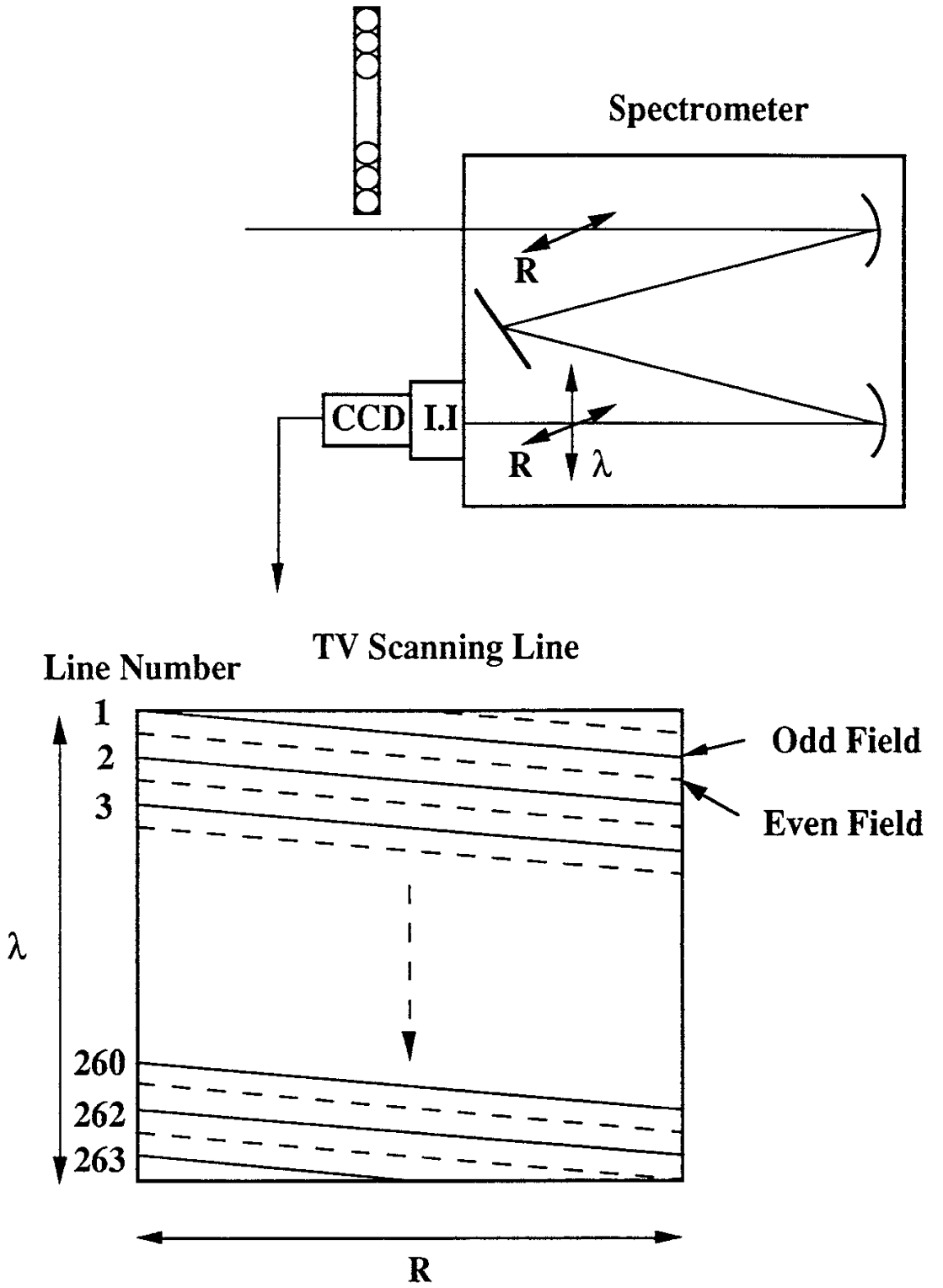
Spectrometer
R
CCD
I.I
R
λ
TV Scanning Line
Line Number
1
2
3
λ
260
262
263
Odd Field
Even Field
R

Fig. 2

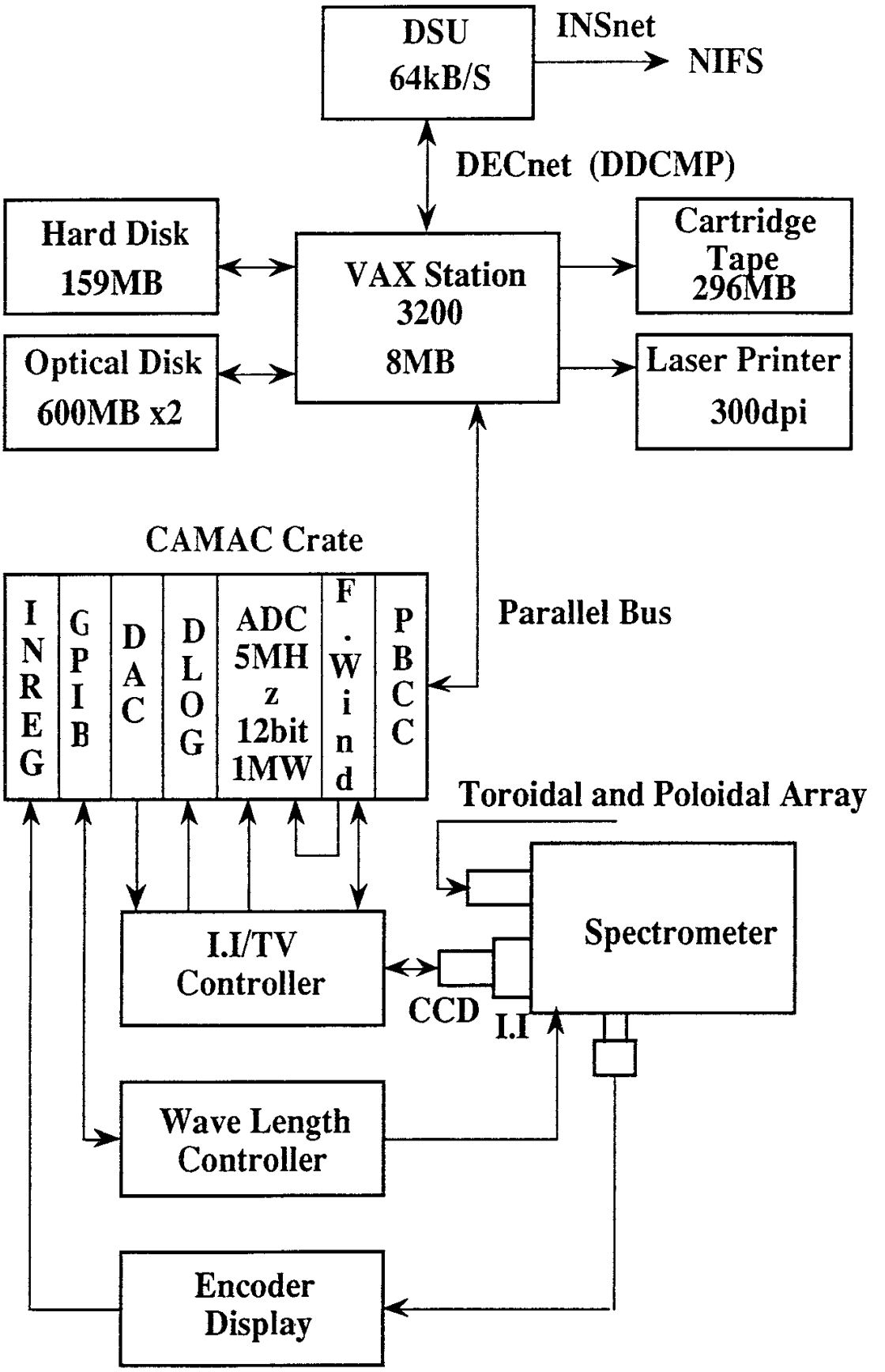
DSU
64kB/S
INSnet
NIFS
DECnet (DDCMP)
Hard Disk
159MB
VAX Station
3200
8MB
Cartridge
Tape
296MB
Optical Disk
600MB x2
Laser Printer
300dpi
CAMAC Crate
INREG
GPIB
DAC
DLOG
ADC
5MH
z
12bit
1MW
F.
Wind
PBCC
Parallel Bus
Toroidal and Poloidal Array
I.I/TV
Controller
CCD
I.I
Spectrometer
Wave Length
Controller
Encoder
Display

Fig.3

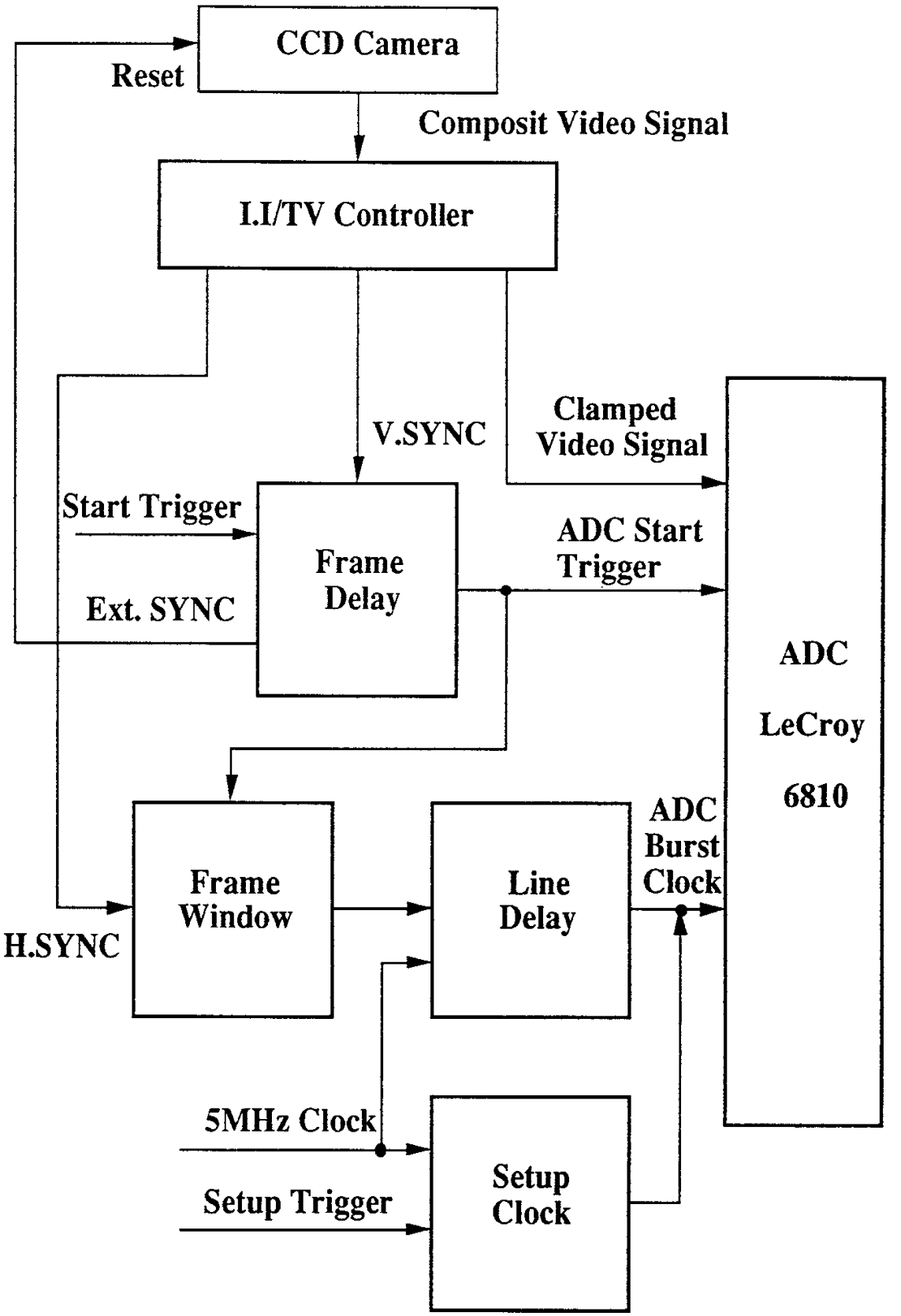
CCD Camera
Reset
Composit Video Signal
I.I/TV Controller
V.SYNC
Clamped
Video Signal
Start Trigger
Frame
Delay
ADC Start
Trigger
Ext. SYNC
ADC
LeCroy
6810
Frame
Window
Line
Delay
ADC
Burst
Clock
H.SYNC
5MHz Clock
Setup Trigger
Setup
Clock

Fig. 4

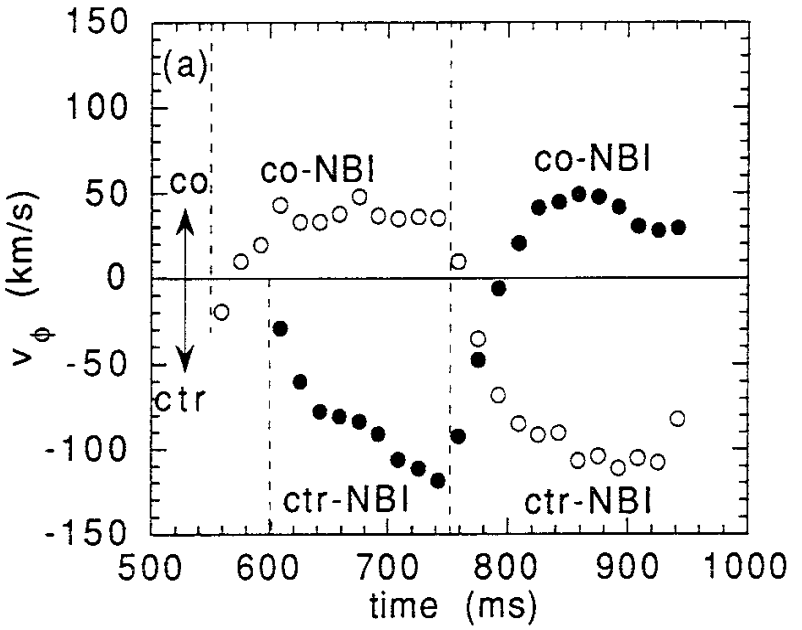
(a)
co
ctr
co-NBI
co-NBI
ctr-NBI
ctr-NBI
v_ϕ (km/s)
time (ms)

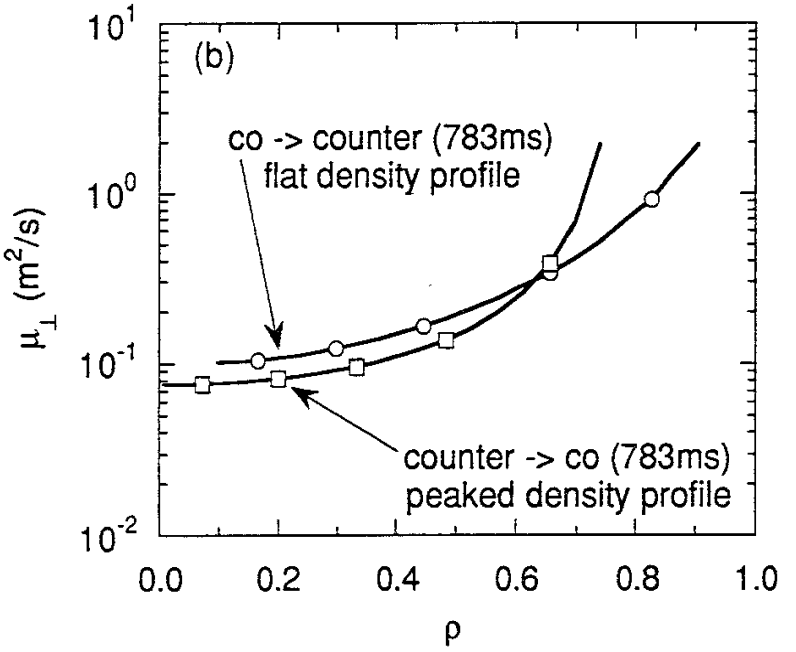
(b)
co -> counter (783ms)
flat density profile
counter -> co (783ms)
peaked density profile
$\mu_\perp$ (m^2/s)
ρ

Fig. 5

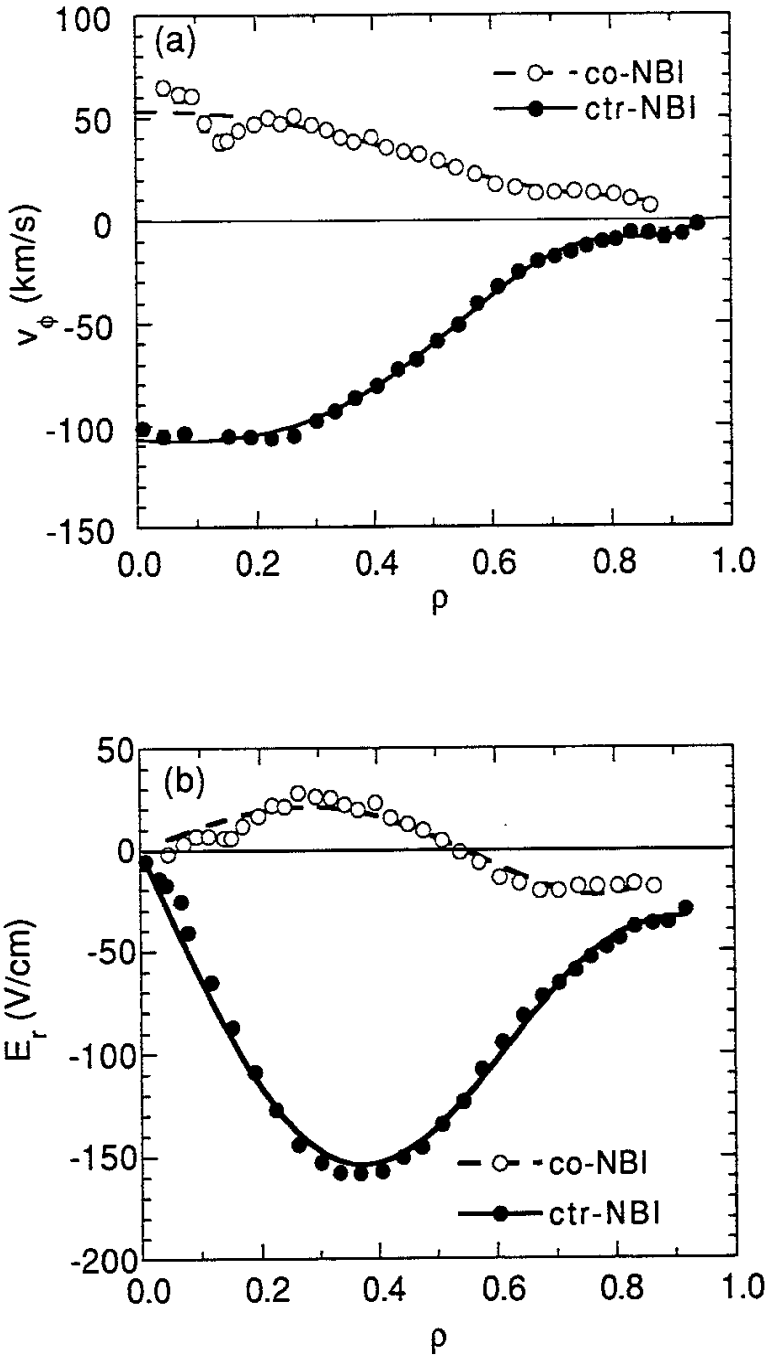
(a)
co-NBI
ctr-NBI
100
50
0
-50
-100
-150
v_ϕ (km/s)
0.0
0.2
0.4
0.6
0.8
1.0
ρ
(b)
50
0
-50
-100
-150
-200
E_r (V/cm)
co-NBI
ctr-NBI
0.0
0.2
0.4
0.6
0.8
1.0
ρ

Fig. 6

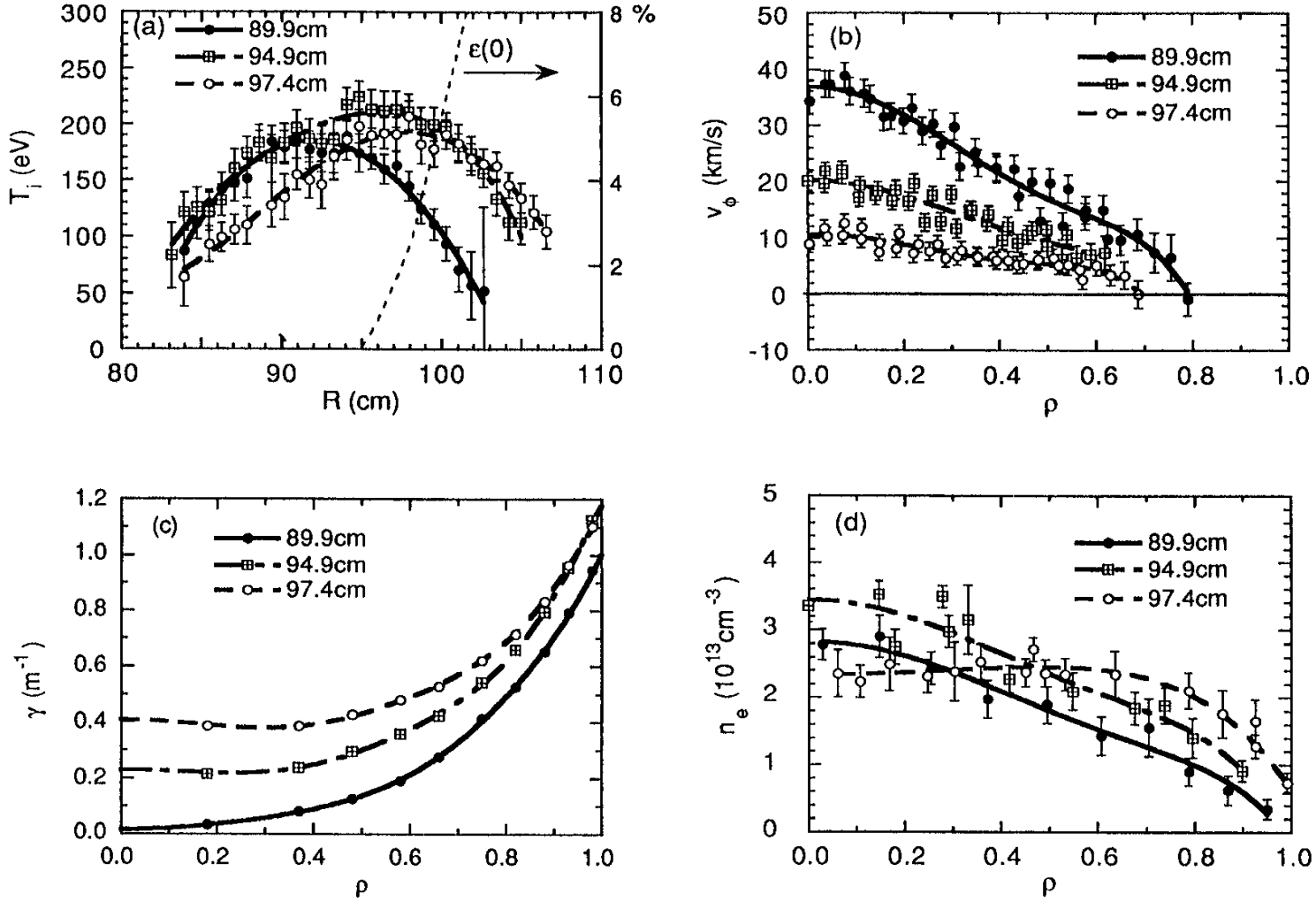

Fig. 7

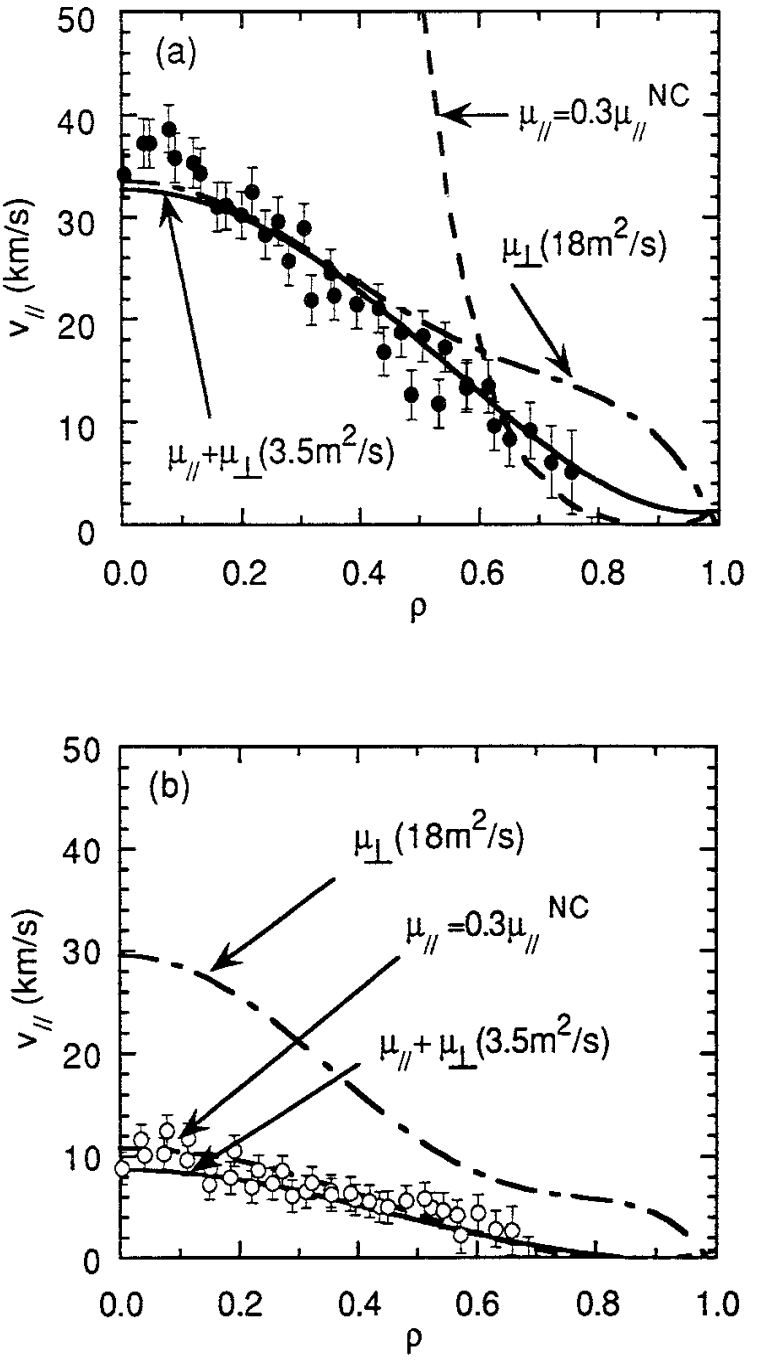
(a)
$\mu_{//}=0.3\mu_{//}^{NC}$
$\mu_\perp(18m^2/s)$
$\mu_{//}+\mu_\perp(3.5m^2/s)$
$v_{//}$ (km/s)
ρ
(b)
$\mu_\perp(18m^2/s)$
$\mu_{//}=0.3\mu_{//}^{NC}$
$\mu_{//}+\mu_\perp(3.5m^2/s)$
$v_{//}$ (km/s)
ρ

Fig. 8

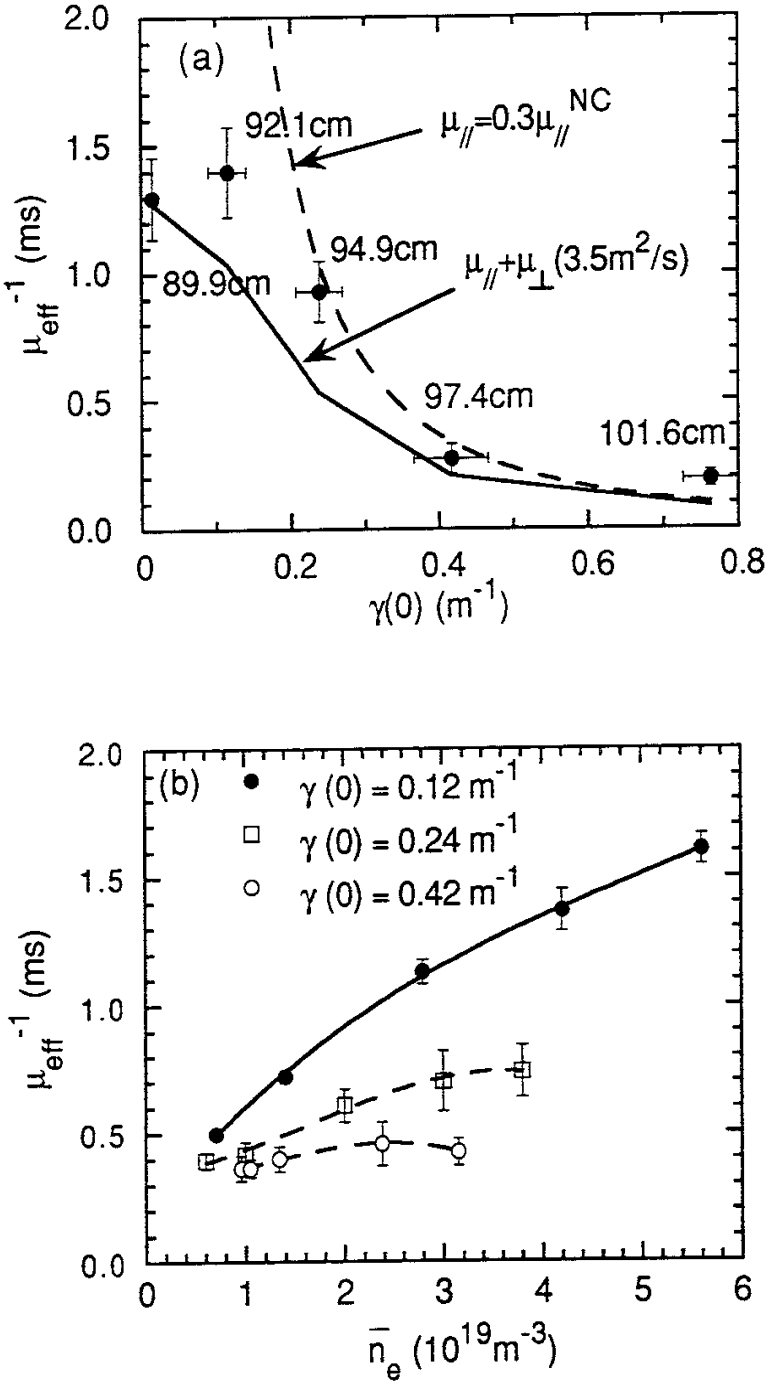
(a)
92.1cm
$\mu_{//}=0.3\mu_{//}^{NC}$
94.9cm
$\mu_{//}+\mu_{\perp}(3.5m^2/s)$
89.9cm
97.4cm
101.6cm
μ_{eff}^{-1} (ms)
$\gamma(0)$ (m^{-1})
(b)
γ (0) = 0.12 m^{-1}
γ (0) = 0.24 m^{-1}
γ (0) = 0.42 m^{-1}
μ_{eff}^{-1} (ms)
$\bar{n}_e$ ($10^{19}m^{-3}$)

Fig. 9

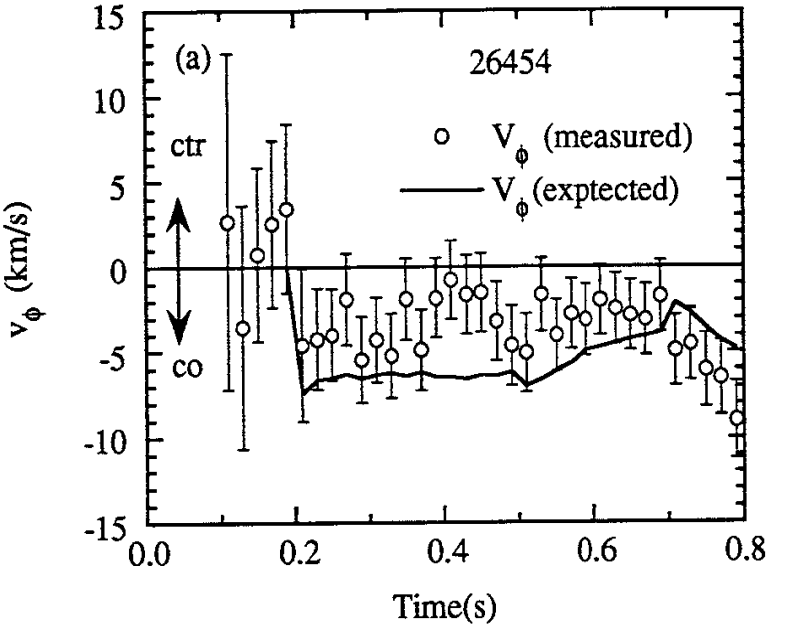
(a)
26454
ctr
co
V_ϕ (measured)
V_ϕ (exptected)
v_ϕ (km/s)
Time(s)
15
10
5
0
-5
-10
-15
0.0
0.2
0.4
0.6
0.8

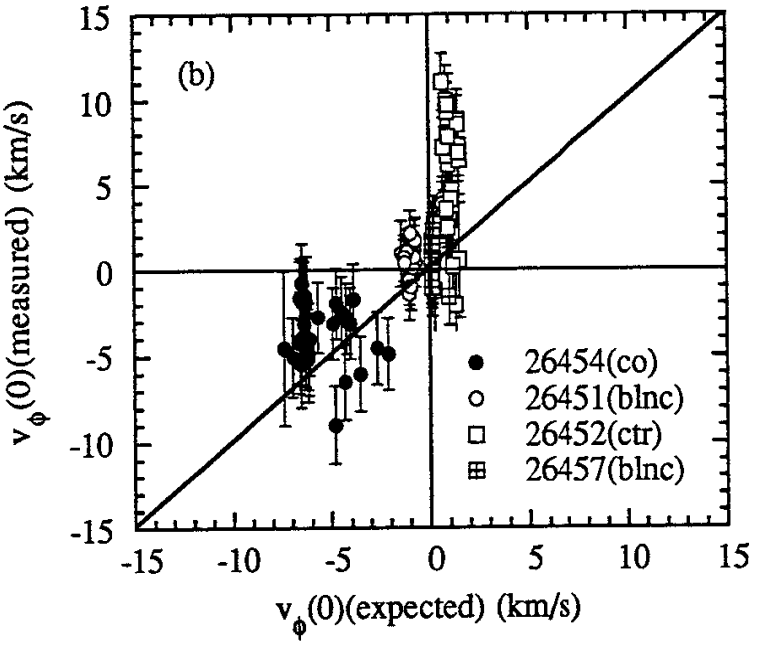
(b)
26454(co)
26451(blnc)
26452(ctr)
26457(blnc)
$v_\phi(0)$(measured) (km/s)
$v_\phi(0)$(expected) (km/s)
15
10
5
0
-5
-10
-15

Fig. 10

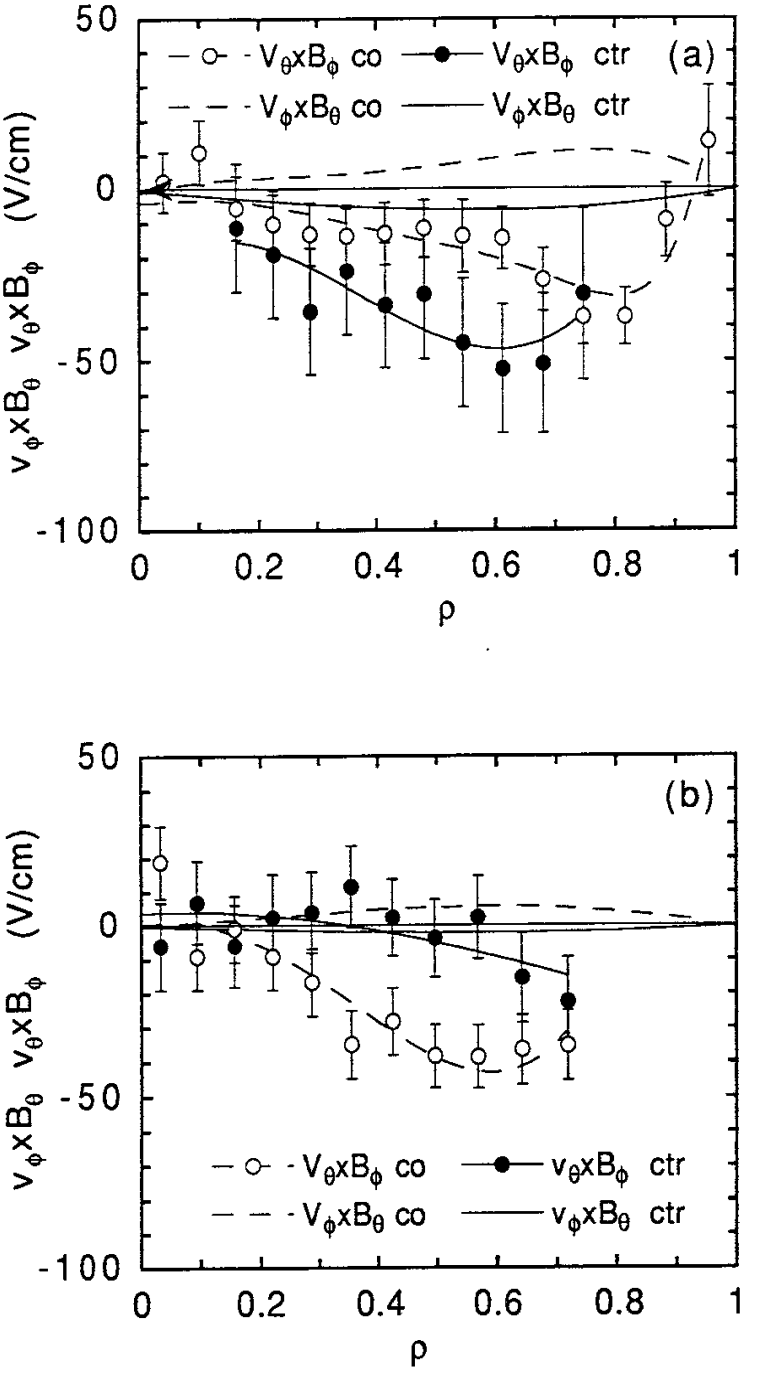
50
0
-50
-100
0
0.2
0.4
0.6
0.8
1
ρ
(V/cm)
$v_\phi xB_\theta$ $v_\theta xB_\phi$
$V_\theta xB_\phi$ co
$V_\theta xB_\phi$ ctr
(a)
$V_\phi xB_\theta$ co
$V_\phi xB_\theta$ ctr
(b)
$v_\theta xB_\phi$ ctr
$v_\phi xB_\theta$ ctr

Fig. 11

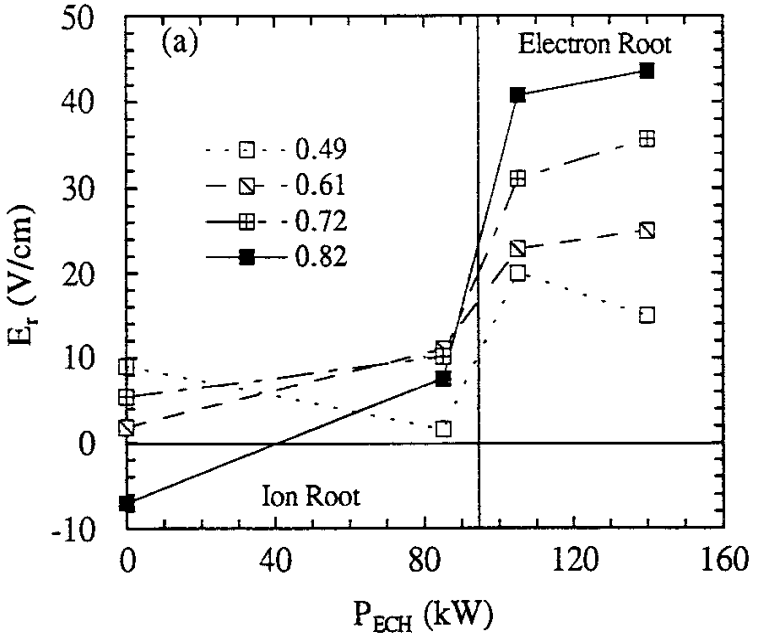
(a)
Electron Root
Ion Root
0.49
0.61
0.72
0.82
E_r (V/cm)
P_{ECH} (kW)
50
40
30
20
10
0
-10
0
40
80
120
160

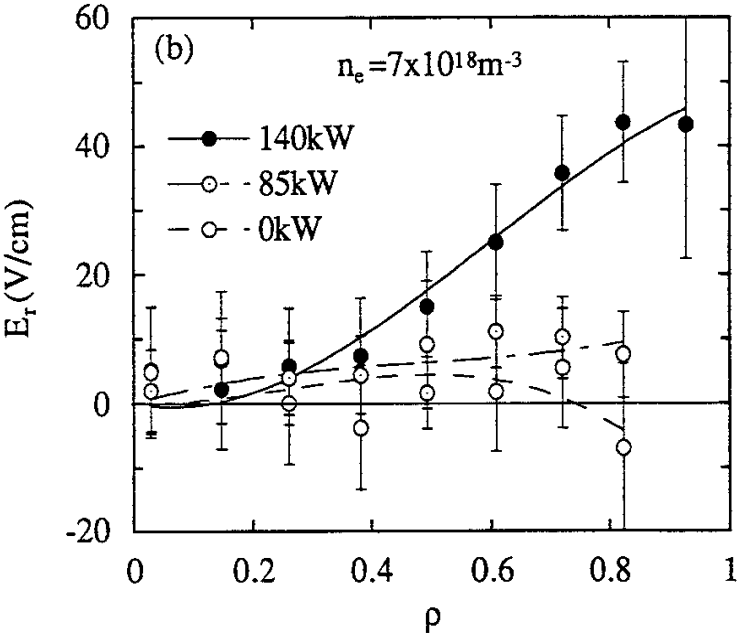
(b)
$n_e=7x10^{18}m^{-3}$
140kW
85kW
0kW
E_r (V/cm)
ρ
60
40
20
0
-20
0
0.2
0.4
0.6
0.8
1

Fig. 12

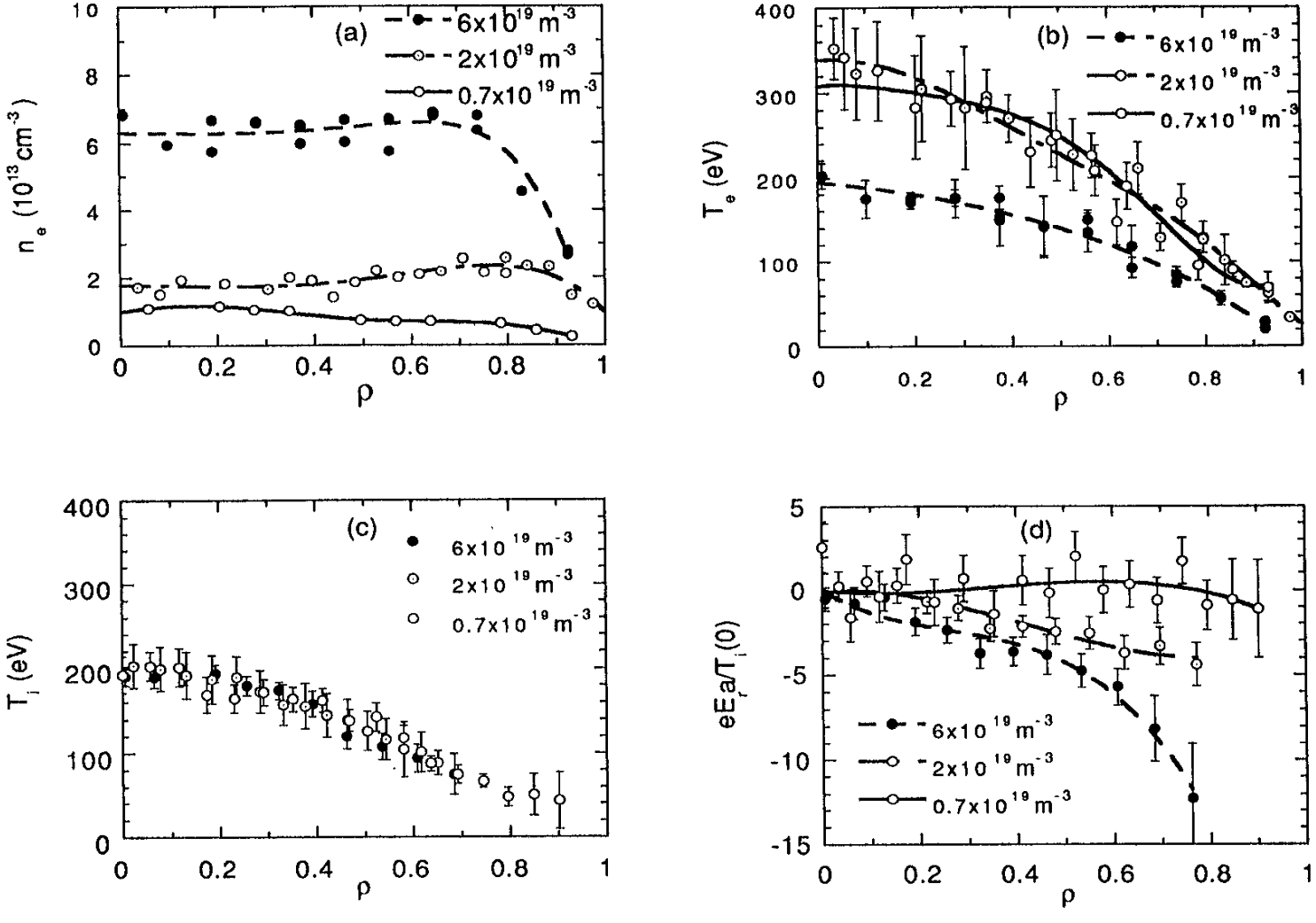
(a)
6x10^19 m^-3
2x10^19 m^-3
0.7x10^19 m^-3
n_e (10^13 cm^-3)
ρ
(b)
T_e (eV)
(c)
T_i (eV)
(d)
eE_r a/T_i(0)

Fig. 13

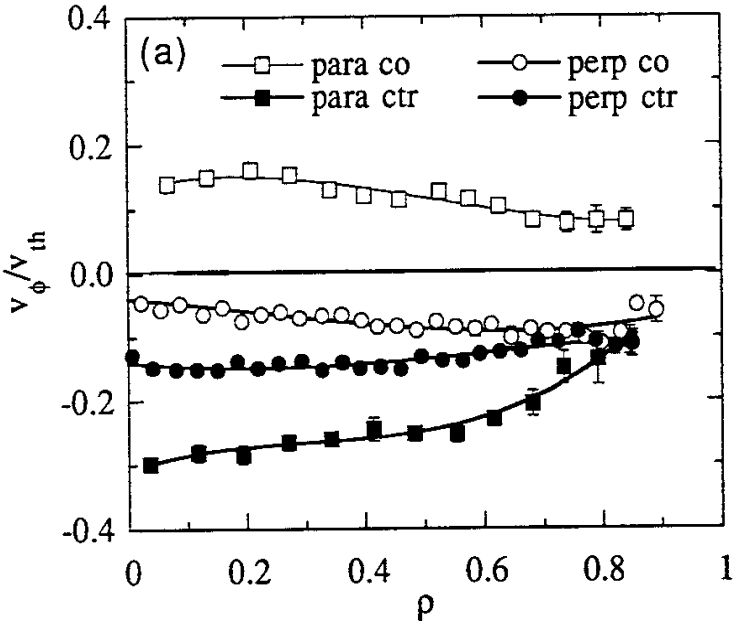
(a)
para co
perp co
para ctr
perp ctr
0.4
0.2
0.0
-0.2
-0.4
v_ϕ/v_{th}
0
0.2
0.4
0.6
0.8
1
ρ

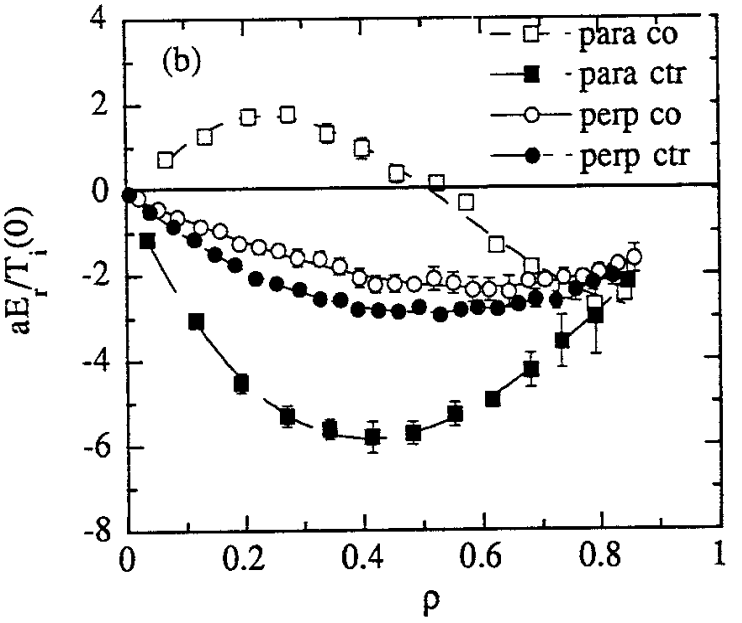
(b)
para co
para ctr
perp co
perp ctr
4
2
0
-2
-4
-6
-8
$aE_r/T_i(0)$
0
0.2
0.4
0.6
0.8
1
ρ

Fig. 14

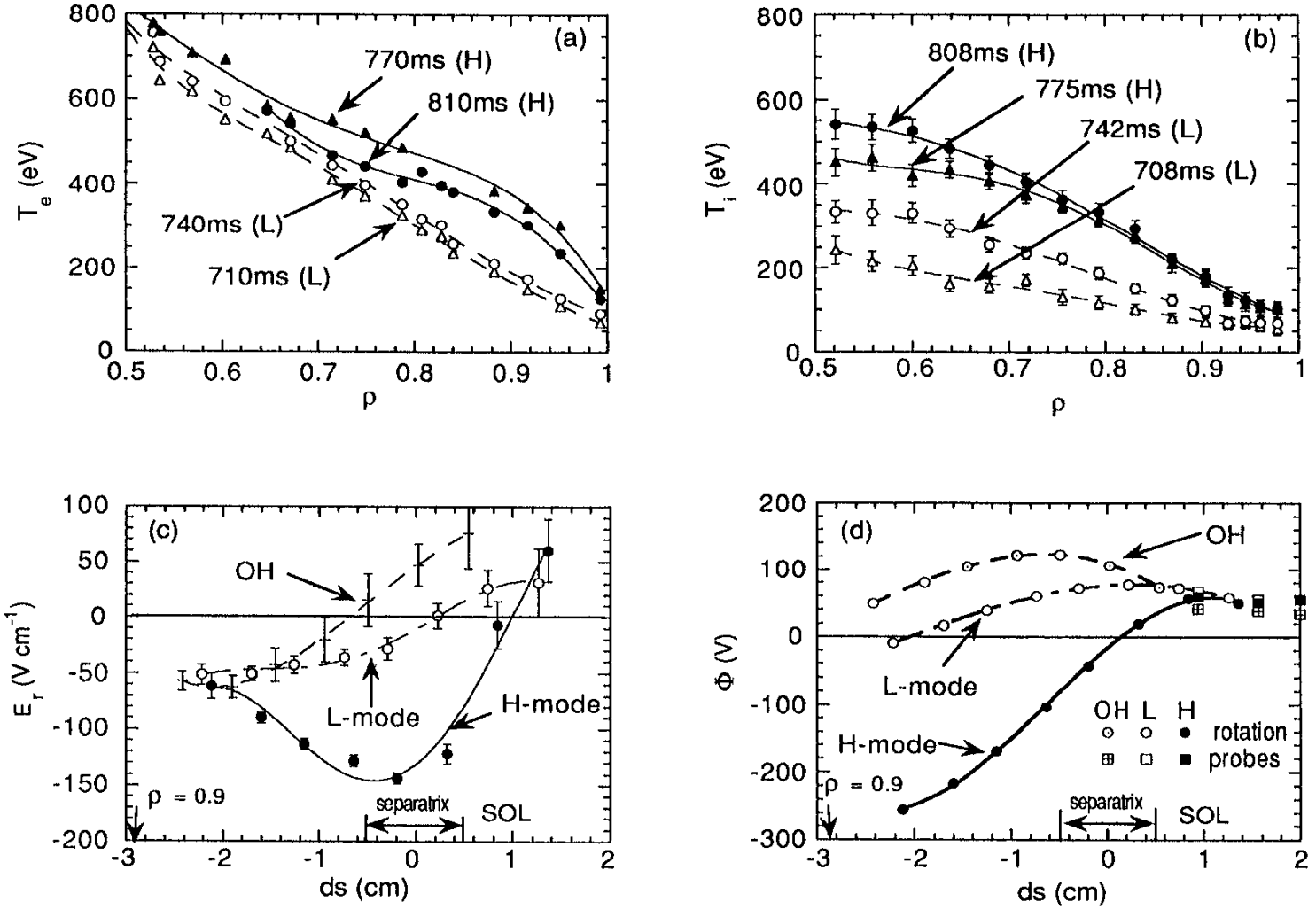
(a)
770ms (H)
810ms (H)
740ms (L)
710ms (L)
T_e (eV)
ρ
(b)
808ms (H)
775ms (H)
742ms (L)
708ms (L)
T_i (eV)
ρ
(c)
OH
L-mode
H-mode
ρ = 0.9
separatrix
SOL
E_r (V cm^{-1})
ds (cm)
(d)
OH
L-mode
H-mode
OH L H
rotation
probes
ρ = 0.9
separatrix
SOL
Φ (V)
ds (cm)

Fig. 15

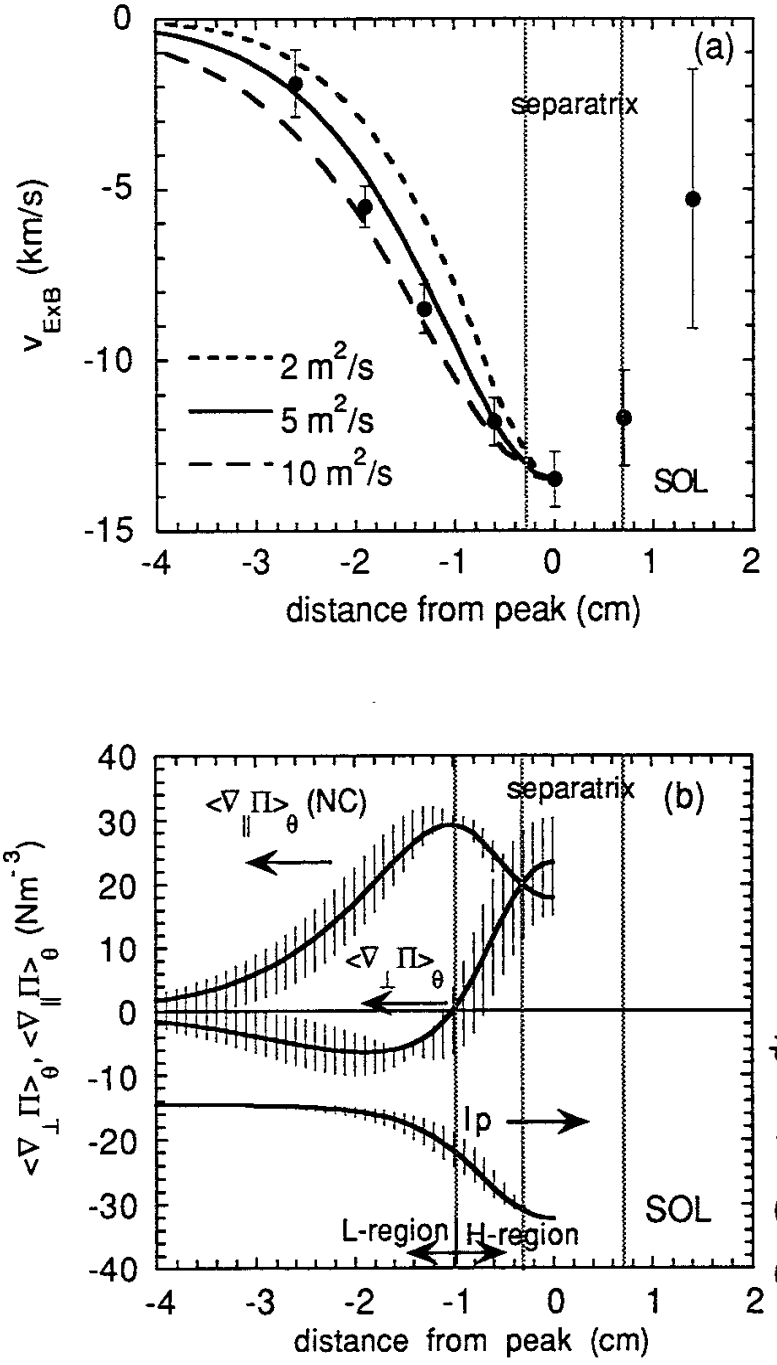
(a)
separatrix
SOL
2 m²/s
5 m²/s
10 m²/s
v_ExB (km/s)
distance from peak (cm)
(b)
separatrix
<∇∥Π>θ (NC)
<∇⊥Π>θ
Ip
SOL
L-region
H-region
<∇⊥Π>θ, <∇∥Π>θ (Nm⁻³)
di
distance from peak (cm)

Fig. 16

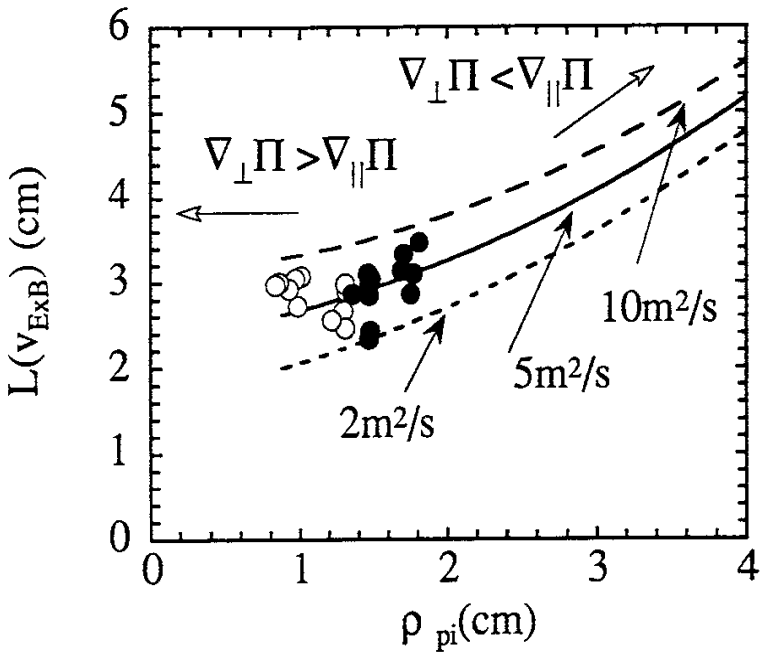
6
5
4
3
2
1
0
0
1
2
3
4
$L(v_{ExB})$ (cm)
ρ_{pi}(cm)
$\nabla_\perp \Pi < \nabla_{||} \Pi$
$\nabla_\perp \Pi > \nabla_{||} \Pi$
10m²/s
5m²/s
2m²/s

Fig. 17

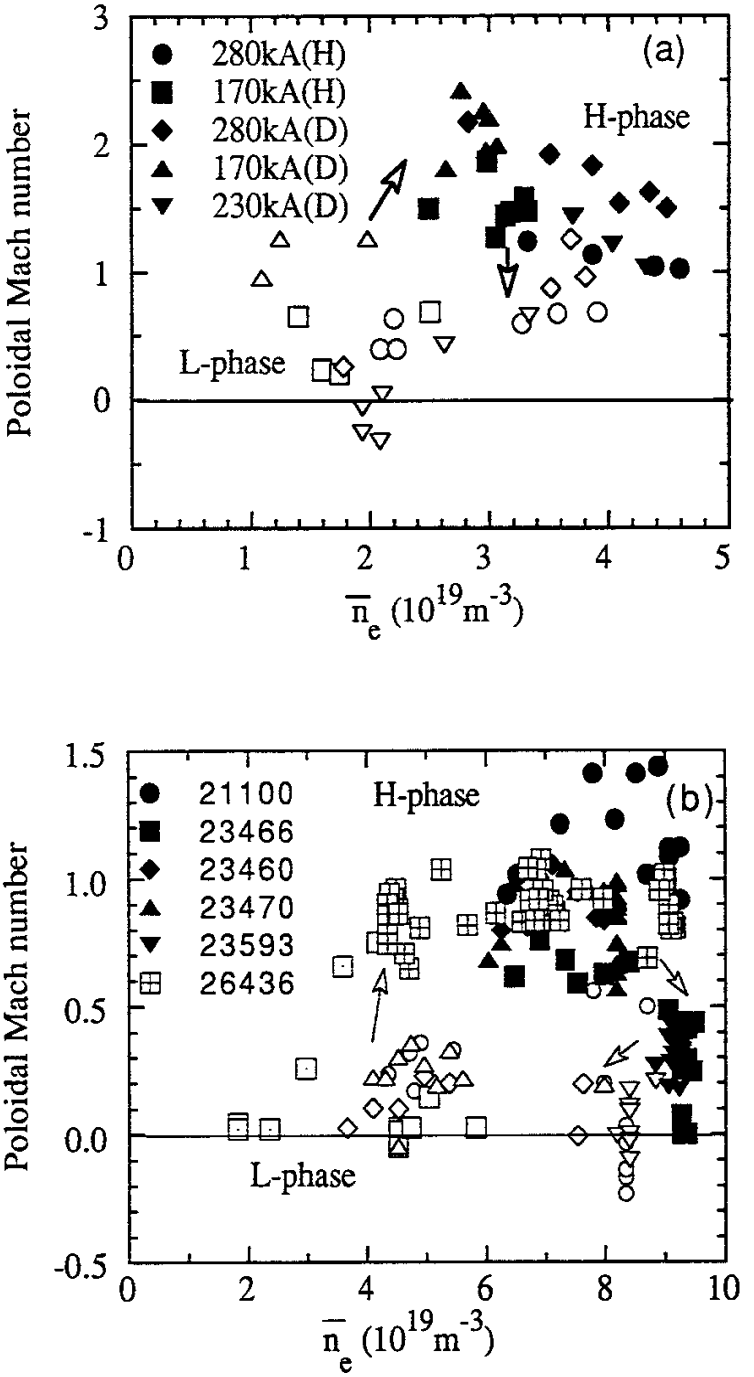
280kA(H)
170kA(H)
280kA(D)
170kA(D)
230kA(D)
(a)
H-phase
L-phase
Poloidal Mach number
$\overline{n}_e$ (10^{19}m^{-3})
21100
23466
23460
23470
23593
26436
(b)
H-phase
L-phase
Poloidal Mach number
$\overline{n}_e$ (10^{19}m^{-3})

Fig. 18

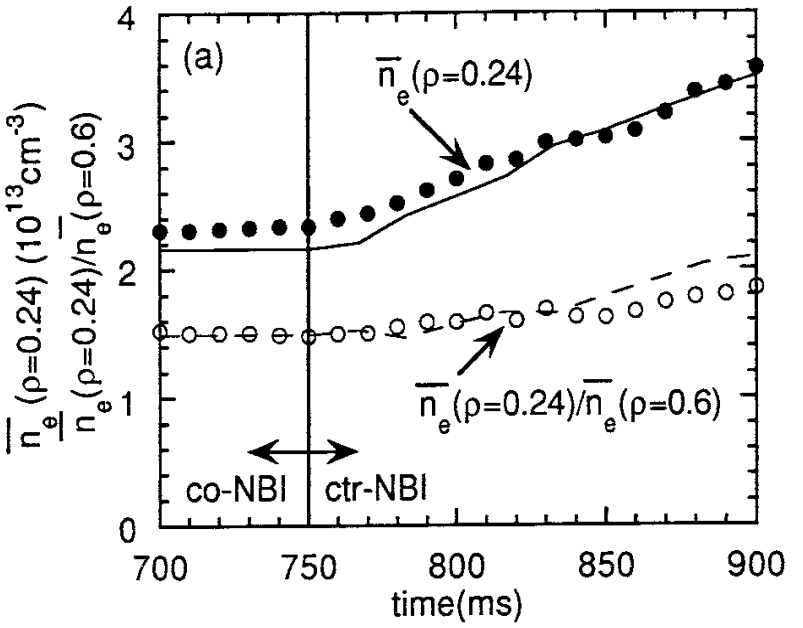
(a)
$\overline{n}_e(\rho=0.24)$
$\overline{n}_e(\rho=0.24)/\overline{n}_e(\rho=0.6)$
co-NBI
ctr-NBI
$\overline{n}_e(\rho=0.24)$ $(10^{13}cm^{-3})$
$\overline{n}_e(\rho=0.24)/\overline{n}_e(\rho=0.6)$
time(ms)

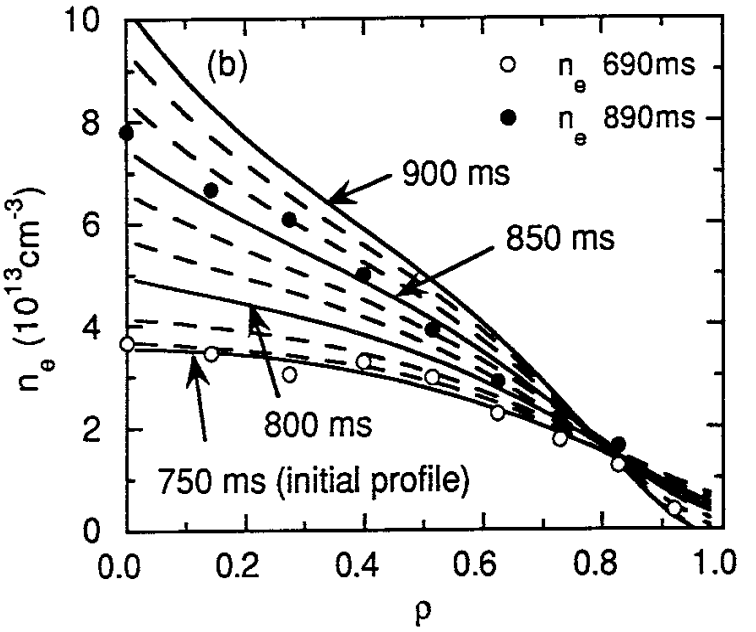
(b)
n_e 690ms
n_e 890ms
900 ms
850 ms
800 ms
750 ms (initial profile)
n_e $(10^{13}cm^{-3})$
ρ

Fig. 19

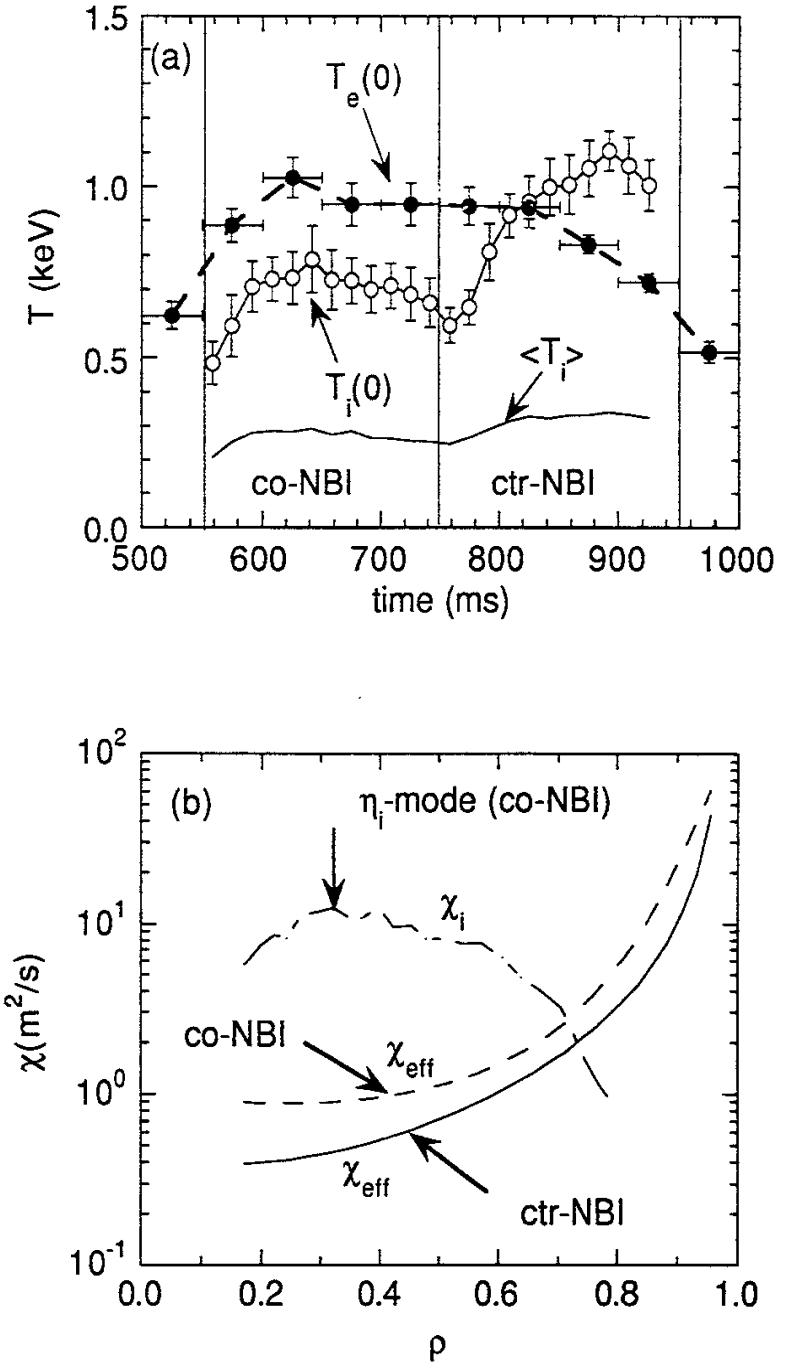
(a)
$T_e(0)$
$T_i(0)$
<T_i>
co-NBI
ctr-NBI
T (keV)
time (ms)
(b)
η_i-mode (co-NBI)
χ_i
co-NBI
χ_{eff}
χ_{eff}
ctr-NBI
$\chi(m^2/s)$
ρ

Fig. 20

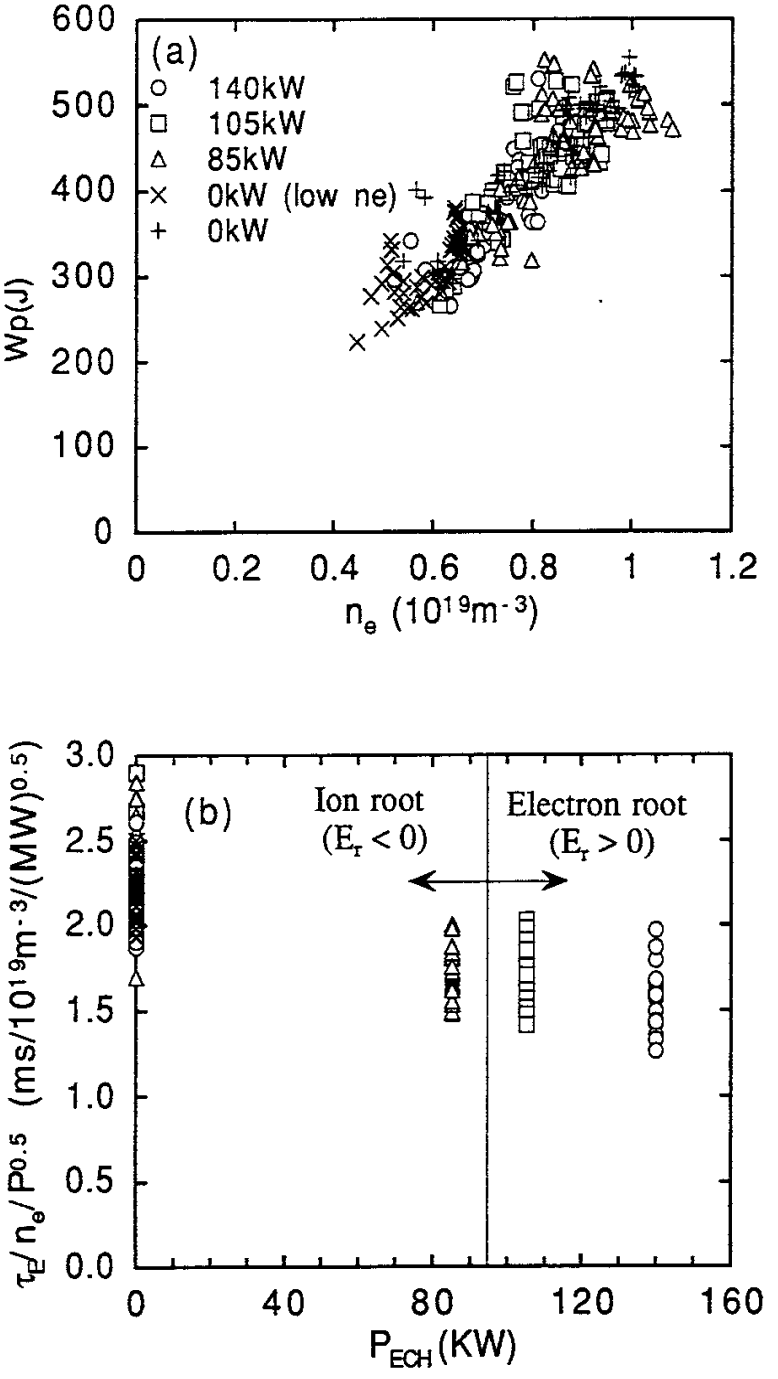
(a)
140kW
105kW
85kW
0kW (low ne)
0kW
Wp(J)
600
500
400
300
200
100
0
0
0.2
0.4
0.6
0.8
1
1.2
n_e ($10^{19}m^{-3}$)
(b)
Ion root
($E_r < 0$)
Electron root
($E_r > 0$)
$\tau_E / n_e / P^{0.5}$ (ms/$10^{19}m^{-3}$/(MW)$^{0.5}$)
3.0
2.5
2.0
1.5
1.0
0.5
0.0
0
40
80
120
160
P_{ECH}(KW)

Fig. 21

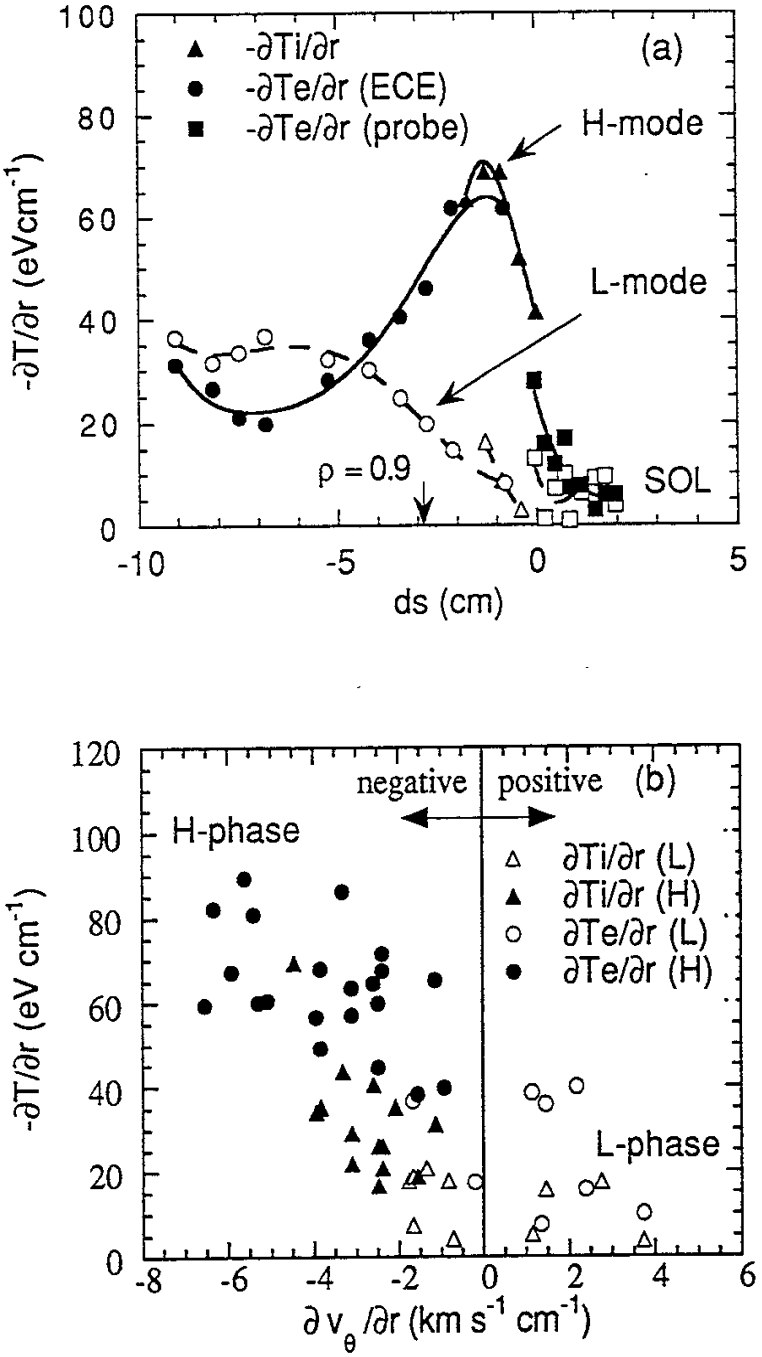
-∂Ti/∂r
-∂Te/∂r (ECE)
-∂Te/∂r (probe)
(a)
H-mode
L-mode
ρ = 0.9
SOL
-∂T/∂r (eVcm^{-1})
ds (cm)
negative
positive
(b)
H-phase
L-phase
∂Ti/∂r (L)
∂Ti/∂r (H)
∂Te/∂r (L)
∂Te/∂r (H)
-∂T/∂r (eV cm^{-1})
∂ v$_\theta$ /∂r (km s^{-1} cm^{-1})

Fig. 22

Recent Issues of NIFS Series

NIFS-274 M. Tanaka,
A Mechanism of Collisionless Magnetic Reconnection; Mar. 1994

NIFS-275 A. Fukuyama, K. Itoh, S.-I. Itoh, M. Yagi and M. Azumi,
Isotope Effect on Confinement in DT Plasmas; Mar. 1994

NIFS-276 R.V. Reddy, K. Watanabe, T. Sato and T.H. Watanabe,
Impulsive Alfven Coupling between the Magnetosphere and Ionosphere; Apr.1994

NIFS-277 J. Uramoto,
A Possibility of π^- Meson Production by a Low Energy Electron Bunch and Positive Ion Bunch; Apr. 1994

NIFS-278 K. Itoh, S.-I. Itoh, A. Fukuyama, M. Yagi and M. Azumi,
Self-sustained Turbulence and L-mode Confinement in Toroidal Plasmas II; Apr. 1994

NIFS-279 K. Yamazaki and K.Y.Watanabe,
New Modular Heliotron System Compatible with Closed Helical Divertor and Good Plasma Confinement; Apr. 1994

NIFS-280 S. Okamura, K. Matsuoka, K. Nishimura, K. Tsumori, R. Akiyama, S. Sakakibara, H. Yamada, S. Morita, T. Morisaki,. N. Nakajima, K. Tanaka, J. Xu, K. Ida, H. Iguchi, A. Lazaros, T. Ozaki, H. Arimoto, A. Ejiri, M. Fujiwara, H. Idei. O. Kaneko, K. Kawahata, T. Kawamoto, A. Komori, S. Kubo, O. Motojima, V.D. Pustovitov, C. Takahashi, K. Toi and I. Yamada,
High-Beta Discharges with Neutral Beam Injection in CHS; Apr. 1994

NIFS-281 K. Kamada, H. Kinoshita and H. Takahashi,
Anomalous Heat Evolution of Deuteron Implanted Al on Electron Bombardment ; May 1994

NIFS-282 H. Takamaru, T. Sato, K. Watanabe and R. Horiuchi,
Super Ion Acoustic Double Layer; May 1994

NIFS-283 O.Mitarai and S. Sudo
Ignition Characteristics in D-T Helical Reactors; June 1994

NIFS-284 R. Horiuchi and T. Sato,
Particle Simulation Study of Driven Magnetic Reconnection in a Collisionless Plasma; June 1994

NIFS-285 K.Y. Watanabe, N. Nakajima, M. Okamoto, K. Yamazaki, Y. Nakamura, M. Wakatani,

Effect of Collisionality and Radial Electric Field on Bootstrap Current in LHD (Large Helical Device); June 1994

NIFS-286 H. Sanuki, K. Itoh, J. Todoroki, K. Ida, H. Idei, H. Iguchi and H. Yamada,
Theoretical and Experimental Studies on Electric Field and Confinement in Helical Systems; June 1994

NIFS-287 K. Itoh and S-I. Itoh,
Influence of the Wall Material on the H-mode Performance; June 1994

NIFS-288 K. Itoh, A. Fukuyama, S.-I. Itoh, M. Yagi and M. Azumi
Self-Sustained Magnetic Braiding in Toroidal Plasmas: July 1994

NIFS-289 Y. Nejoh,
Relativistic Effects on Large Amplitude Nonlinear Langmuir Waves in a Two-Fluid Plasma; July 1994

NIFS-290 N. Ohyabu, A. Komori, K. Akaishi, N. Inoue, Y. Kubota, A.I. Livshit, N. Noda, A. Sagara, H. Suzuki, T. Watanabe, O. Motojima, M. Fujiwara, A. Iiyoshi,
Innovative Divertor Concepts for LHD; July 1994

NIFS-291 H. Idei, K. Ida, H. Sanuki, S. Kubo, H. Yamada, H. Iguchi, S. Morita, S. Okamura, R. Akiyama, H. Arimoto, K. Matsuoka, K. Nishimura, K. Ohkubo, C. Takahashi, Y. Takita, K. Toi, K. Tsumori and I. Yamada,
Formation of Positive Radial Electric Field by Electron Cyclotron Heating in Compact Helical System; July 1994

NIFS-292 N. Noda, A. Sagara, H. Yamada, Y. Kubota, N. Inoue, K. Akaishi, O. Motojima, K. Iwamoto, M. Hashiba, I. Fujita, T. Hino, T. Yamashina, K. Okazaki, J. Rice, M. Yamage, H. Toyoda and H. Sugai,
Boronization Study for Application to Large Helical Device; July 1994

NIFS-293 Y. Ueda, T. Tanabe, V. Philipps, L. Könen, A. Pospieszczyk, U. Samm, B. Schweer, B. Unterberg, M. Wada, N. Hawkes and N. Noda,
Effects of Impurities Released from High Z Test Limiter on Plasma Performance in TEXTOR; July. 1994

NIFS-294 K. Akaishi, Y. Kubota, K. Ezaki and O. Motojima,
Experimental Study on Scaling Law of Outgassing Rate with A Pumping Parameter, Aug. 1994

NIFS-295 S. Bazdenkov, T. Sato, R. Horiuchi, K. Watanabe
Magnetic Mirror Effect as a Trigger of Collisionless Magnetic Reconnection, Aug. 1994

NIFS-296 K. Itoh, M. Yagi, S.-I. Itoh, A. Fukuyama, H. Sanuki, M. Azumi
Anomalous Transport Theory for Toroidal Helical Plasmas,

Aug. 1994 (IAEA-CN-60/D-III-3)

NIFS-297 J. Yamamoto, O. Motojima, T. Mito, K. Takahata, N. Yanagi, S. Yamada, H. Chikaraishi, S. Imagawa, A. Iwamoto, H. Kaneko, A. Nishimura, S. Satoh, T. Satow, H. Tamura, S. Yamaguchi, K. Yamazaki, M. Fujiwara, A. Iiyoshi and LHD group,
New Evaluation Method of Superconductor Characteristics for Realizing the Large Helical Device; Aug. 1994 (IAEA-CN-60/F-P-3)

NIFS-298 A. Komori, N. Ohyabu, T. Watanabe, H. Suzuki, A. Sagara, N. Noda, K. Akaishi, N. Inoue, Y. Kubota, O Motojima, M. Fujiwara and A. Iiyoshi,
Local Island Divertor Concept for LHD; Aug. 1994 (IAEA-CN-60/F-P-4)

NIFS-299 K. Toi, T. Morisaki, S. Sakakibara, A. Ejiri, H. Yamada, S. Morita, K. Tanaka, N. Nakajima, S. Okamura, H. Iguchi, K. Ida, K. Tsumori, S. Ohdachi, K. Nishimura, K. Matsuoka, J. Xu, I. Yamada, T. Minami, K. Narihara, R. Akiyama, A. Ando, H. Arimoto, A. Fujisawa, M. Fujiwara, H. Idei, O. Kaneko, K. Kawahata, A. Komori, S. Kubo, R. Kumazawa, T. Ozaki, A. Sagara, C. Takahashi, Y. Takita and T. Watari
Impact of Rotational-Transform Profile Control on Plasma Confinement and Stability in CHS; Aug. 1994 (IAEA-CN-60/A6/C-P-3)

NIFS-300 H. Sugama and W. Horton,
Dynamical Model of Pressure-Gradient-Driven Turbulence and Shear Flow Generation in L-H Transition; Aug. 1994 (IAEA/CN-60/D-P-I-11)

NIFS-301 Y. Hamada, A. Nishizawa, Y. Kawasumi, K.N. Sato, H. Sakakita, R. Liang, K. Kawahata, A. Ejiri, K. Narihara, K. Sato, T. Seki, K. Toi, K. Itoh, H. Iguchi, A. Fujisawa, K. Adachi, S. Hidekuma, S. Hirokura, K. Ida, M. Kojima, J. Koog, R. Kumazawa, H. Kuramoto, T. Minami, I. Negi, S. Ohdachi, M. Sasao, T. Tsuzuki, J. Xu, I. Yamada, T. Watari,
Study of Turbulence and Plasma Potential in JIPP T-IIU Tokamak;
Aug. 1994 (IAEA/CN-60/A-2-III-5)

NIFS-302 K. Nishimura, R. Kumazawa, T. Mutoh, T. Watari, T. Seki, A. Ando, S. Masuda, F. Shinpo, S. Murakami, S. Okamura, H. Yamada, K. Matsuoka, S. Morita, T. Ozaki, K. Ida, H. Iguchi, I. Yamada, A. Ejiri, H. Idei, S. Muto, K. Tanaka, J. Xu, R. Akiyama, H. Arimoto, M. Isobe, M. Iwase, O. Kaneko, S. Kubo, T. Kawamoto, A. Lazaros, T. Morisaki, S. Sakakibara, Y. Takita, C. Takahashi and K. Tsumori,
ICRF Heating in CHS; Sep. 1994 (IAEA-CN-60/A-6-I-4)

NIFS-303 S. Okamura, K. Matsuoka, K. Nishimura, K. Tsumori, R. Akiyama, S. Sakakibara, H. Yamada, S. Morita, T. Morisaki, N. Nakajima, K. Tanaka, J. Xu, K. Ida, H. Iguchi, A. Lazaros, T. Ozaki, H. Arimoto, A. Ejiri, M. Fujiwara, H. Idei, A. Iiyoshi, O, Kaneko, K. Kawahata, T. Kawamoto, S. Kubo, T. Kuroda, O. Motojima, V.D. Pustovitov, A. Sagara, C. Takahashi, K. Toi and I. Yamada,

High Beta Experiments in CHS; Sep. 1994 (IAEA-CN-60/A-2-IV-3)

NIFS-304 K. Ida, H. Idei, H. Sanuki, K. Itoh, J. Xu, S. Hidekuma, K. Kondo, A. Sahara, H. Zushi, S.-I. Itoh, A. Fukuyama, K. Adati, R. Akiyama, S. Bessho, A. Ejiri, A. Fujisawa, M. Fujiwara, Y. Hamada, S. Hirokura, H. Iguchi, O. Kaneko, K. Kawahata, Y. Kawasumi, M. Kojima, S. Kubo, H. Kuramoto, A. Lazaros, R. Liang, K. Matsuoka, T. Minami, T. Mizuuchi, T. Morisaki, S. Morita, K. Nagasaki, K. Narihara, K. Nishimura, A. Nishizawa, T. Obiki, H. Okada, S. Okamura, T. Ozaki, S. Sakakibara, H. Sakakita, A. Sagara, F. Sano, M. Sasao, K. Sato, K.N. Sato, T. Saeki, S. Sudo, C. Takahashi, K. Tanaka, K. Tsumori, H.Yamada, I. Yamada, Y. Takita, T. Tuzuki, K. Toi and T. Watari, *Control of Radial Electric Field in Torus Plasma;* Sep. 1994 (IAEA-CN-60/A-2-IV-2)

NIFS-305 T. Hayashi, T. Sato, N. Nakajima, K. Ichiguchi, P. Merkel, J. Nührenberg, U. Schwenn, H. Gardner, A. Bhattacharjee and C.C.Hegna, *Behavior of Magnetic Islands in 3D MHD Equilibria of Helical Devices*; Sep. 1994 (IAEA-CN-60/D-2-II-4)

NIFS-306 S. Murakami, M. Okamoto, N. Nakajima, K.Y. Watanabe, T. Watari, T. Mutoh, R. Kumazawa and T. Seki, *Monte Carlo Simulation for ICRF Heating in Heliotron/Torsatrons*; Sep. 1994 (IAEA-CN-60/D-P-I-14)

NIFS-307 Y. Takeiri, A. Ando, O. Kaneko, Y. Oka, K. Tsumori, R. Akiyama, E. Asano, T. Kawamoto, T. Kuroda, M. Tanaka and H. Kawakami *Development of an Intense Negative Hydrogen Ion Source with a Wide-Range of External Magnetic Filter Field*; Sep. 1994

NIFS-308 T. Hayashi, T. Sato, H.J. Gardner and J.D. Meiss, *Evolution of Magnetic Islands in a Heliac*; Sep. 1994

NIFS-309 H. Amo, T. Sato and A. Kageyama, *Intermittent Energy Bursts and Recurrent Topological Change of a Twisting Magnetic Flux Tube*; Sep.1994

NIFS-310 T. Yamagishi and H. Sanuki, *Effect of Anomalous Plasma Transport on Radial Electric Field in Torsatron/Heliotron*; Sep. 1994

NIFS-311 K. Watanabe, T. Sato and Y. Nakayama, *Current-profile Flattening and Hot Core Shift due to the Nonlinear Development of Resistive Kink Mode*; Oct. 1994

NIFS-312 M. Salimullah, B. Dasgupta, K. Watanabe and T. Sato, *Modification and Damping of Alfvén Waves in a Magnetized Dusty Plasma*; Oct. 1994